

Dynamical Evolution of Galaxies in Clusters

Oleg Y. Gnedin

Princeton University Observatory, Princeton, NJ 08544¹

ABSTRACT

Tidal forces acting on galaxies in clusters lead to a strong dynamical evolution. In order to quantify the amount of evolution, I run self-consistent N -body simulations of disk galaxies for a variety of models in the hierarchically forming clusters. The tidal field along the galactic orbits is extracted from the simulations of cluster formation in the $\Omega_0 = 1$; $\Omega_0 = 0.4$; and $\Omega_0 = 0.4$, $\Omega_\Lambda = 0.6$ cosmological scenarios. For large spiral galaxies with the rotation speed of 250 km s^{-1} , tidal interactions truncate massive dark matter halos at $30 \pm 6 \text{ kpc}$, and thicken stellar disks by a factor 2 to 3, increasing Toomre's parameter to $Q \gtrsim 2$ and halting star formation. Low density galaxies, such as the dwarf spheroidals with the circular velocity of 20 km s^{-1} and the extended low surface brightness galaxies with the scale length of $10 - 15 \text{ kpc}$, are completely disrupted by tidal shocks. Their debris contribute to the diffuse intracluster light. The tidal effects are significant not only in the core but throughout the cluster and can be parametrized by the critical tidal density. The tidally-induced evolution results in the transformation of the infalling spirals into S0 galaxies and in the depletion of the LSB population. In the low Ω_0 cosmological models, clusters form earlier and produce stronger evolution of galaxies.

Subject headings: stellar dynamics — galaxies: clusters: general — galaxies: evolution — galaxies: interactions — methods: N -body simulations

1. Introduction

Hierarchical formation of clusters of galaxies involves strong local variations of the potential field. These tidal perturbations affect the dynamics of infalling disk galaxies in a number of ways. Firstly, they lead to the truncation of stellar and dark matter distributions at a critical radius of the Roche lobe. Secondly, they increase the stellar energy and the amount of random motion in the disk. Tidal heating may be strong enough to completely unbind small galaxies and significantly transform larger ones. Also, tidal heating is likely to stabilize stellar disks against gravitational instability and suppress subsequent star formation. The result of all these effects may be the morphological transformation of a spiral galaxy to an S0 type.

Such transformation is indeed revealed by the

photometric and spectroscopic studies of clusters of galaxies at various redshifts (Jones, Smail & Couch 2000, and references therein). While the fraction of elliptical galaxies stays roughly the same, the abundance of spirals decreases by a factor of 2 to 3 from redshift 0.5 to the present. Correspondingly, the number of S0 galaxies grows by the same amount.

In Gnedin (2003; hereafter Paper I) I have argued that an important role in such a transformation is played by the tidal interactions of galaxies with their massive neighbors and with the global cluster halo. Using numerical simulations of the representative clusters of galaxies in three different cosmological scenarios, I have estimated the amount of tidal heating of the infalling galaxies. The main contribution comes from the interaction with the structures of order 100 kpc in size.

Previous studies (Richstone 1976; Farouki & Shapiro 1981; and especially, Moore et al. 1998, 1999; see more references in Paper I) have shown

¹Present address: Space Telescope Science Institute, 3700 San Martin Drive, Baltimore, MD 21218; ognedin@stsci.edu

that close encounters between disk galaxies can significantly modify their structure and leave behind the distorted spheroidals. The interaction of galaxies with the cluster halo has also been studied (Merritt 1984) in the case of static spherical cluster models. This leads to the tidal truncation of galaxies.

In this paper, I investigate the dynamical effects of tidal heating of disk galaxies in the hierarchically forming clusters. I use a high-resolution self-consistent N -body code to resimulate a sample of galaxies from the lower resolution cosmological simulations described in Paper I. The changes in stellar orbits result from the effects of external tidal fields, computed from the second spatial derivative of the cluster potential along the galaxy trajectories. The fast variation of the tidal force produces tidal shocks responsible for the truncation of galactic halos and the kinematic heating of stars. In agreement with the estimates of Paper I, I find stronger tidal heating in the low Ω_0 cosmological scenario.

I use analytical arguments and discuss the expected evolution of galaxies via tidal heating in §2. In §3, I describe the selection of the sample of galaxies from the cluster simulations. In §4, I present the numerical method and the tests of numerical relaxation. Then I describe the evolution of large spiral galaxies in §5, including the possible effects on the gas. The disruption of dwarf and low surface brightness galaxies in §6 leads to the discussion of the origin of intracluster light. I compare these results with the previous studies in §7 and discuss their observational implications in §8.

2. The Critical Tidal Density

Let us start with an analytic estimate to indicate the range of systems where tidal forces are important. The external tidal force is $-(d^2\Phi/dr_\alpha dr_\beta)_0 r_\beta \equiv F_{\alpha\beta} r_\beta$. The amplitude of the tidal field relates directly to the tidal stripping density, which is analogous to the instantaneous density of the Roche lobe around galaxies but depends on the highest tidal peaks along the galactic orbit. If a part of the galaxy has lower density than the critical value, it would be stripped or torn apart. From Poisson's equation, the trace of the tidal tensor is $F_{\text{tid}} \equiv F_{\alpha\alpha} = 4\pi G\rho_{\text{tid}}$. A typical value of the

tidal peaks in Paper I is $F_{\text{tid}} \sim 100 \text{ Gyr}^{-2}$, and the corresponding tidal density is

$$\rho_{\text{tid}} = 1.8 \times 10^{-3} \left(\frac{F_{\text{tid}}}{100 \text{ Gyr}^{-2}} \right) M_\odot \text{ pc}^{-3}. \quad (1)$$

This should be compared with the combined average density $\rho_{\text{av}} \equiv M(r)/(4\pi r^3/3)$ of stars and dark matter in a galaxy.

Consider a Milky Way-type galaxy with a large isothermal halo and an exponential disk (as in §4.1). The average halo density at the core radius is $\rho_{h,\text{av}}(R_c) \approx 0.74 \sigma_{250}^2 R_{c,\text{kpc}}^{-2} M_\odot \text{ pc}^{-3}$, where σ_{250} is the velocity dispersion in units of 250 km s^{-1} . The average disk density at one scale length is $\rho_{d,\text{av}}(R_0) \approx 0.63 M_{d,10} R_{0,\text{kpc}}^{-3} M_\odot \text{ pc}^{-3}$, where $M_{d,10}$ is the disk mass in units of $10^{10} M_\odot$. Thus the inner regions of large spiral galaxies are stable against tidal disruption.

Extended halos, falling outside the Roche lobe, would be truncated at a radius R_t such that $\rho_{\text{av}}(R_t) \approx \rho_{\text{tid}}$. For our models this corresponds to the tidal radius $R_t \approx 42 \sigma_{250} \text{ kpc}$. In addition to the instantaneous stripping, secular tidal heating would enhance the mass loss. Stellar disks with $R_0 \sim 3 \text{ kpc}$ are better protected – 99% of their mass is within the tidal radius.

On other hand, low surface brightness galaxies (including the dwarf spheroidals) are in danger of being disrupted by tidal forces. The LSB galaxies have lower density than normal spirals, $\lesssim 10^{-2} M_\odot \text{ pc}^{-3}$, and are dominated by dark matter at all radii. Thus their disks would hold as long as they are being protected by the halos. Even though the halo velocity dispersions are similar to those in large spiral galaxies, the larger sizes imply lower density and so stronger truncation. Stirred further by tidal shocks, the LSB galaxies would lose most of their mass, leaving behind extended tidal streams of stars and dark matter. These qualitative arguments are supported by detailed simulations in §5 and §6.

2.1. Stripping of Dark Matter Halos

The total amount of dark matter stripped from the galaxies can be estimated analytically in the spirit of Merritt (1984). Assume that all mass of the cluster belonged initially to the galaxies, distributed according to the Schechter luminosity

function

$$N(L) dL = N_0 \left(\frac{L}{L_*} \right)^{-\alpha} e^{-L/L_*} \frac{dL}{L_*}, \quad (2)$$

with $\alpha \approx 1$. Let the mass-to-light ratio be constant and use the Faber–Jackson (1976) relation for the velocity dispersion, $\sigma_g = \sigma_{g,*} (L/L_*)^{1/4}$. The characteristic break of the luminosity function, L_* , corresponds to the mass scale $M_* \approx 5 \times 10^{12} h^{-1} M_\odot$. Finally, assume that the density profiles of the galaxies and the cluster are isothermal with the three-dimensional velocity dispersions σ_g and σ_{cl} , respectively. The characteristic values in the simulations of Paper I are $\sigma_g = 250 \text{ km s}^{-1}$ and $\sigma_{cl} = \sqrt{3} \times 660 \text{ km s}^{-1}$. Then the galactic halos will be truncated at

$$R_t \approx \frac{\sigma_g}{\sigma_{cl}} R_p, \quad (3)$$

where R_p is the distance of closest approach to the cluster center (pericenter). For many galaxies this distance is of the order the cluster core radius, $R_p \sim 200 \text{ kpc}$, which gives the truncation radius $R_t \approx 44 \text{ kpc}$. The halo mass is then reduced to

$$M_t \approx \frac{1}{G} \frac{\sigma_g^3}{\sigma_{cl}} R_p \approx 6.3 \times 10^{11} M_\odot. \quad (4)$$

Tidal truncation modifies the mass function of galaxies such that the effective exponential cut-off occurs at M_t instead of M_* . Merritt (1984) estimates the fraction of mass remaining bound to the galaxies as $0.7 M_t/M_*$, or about 6% in our case. Tidal heating would further reduce the mass of the galaxies.

For a massive cluster CL 0024+1654, Tyson, Kochanski & Dell’Antonio (1998) were able to infer the mass distribution using image reconstruction of the strong gravitational lensing. The potential of the cluster appears to be very smooth, with only 2% of the mass bound to luminous galaxies. This is consistent with our estimate, as the velocity dispersion of CL 0024+1654 is twice that of our clusters. Thus even if the galaxies contained all of the cluster mass initially, they would retain only a small fraction of it after tidal stripping.

3. Constructing the Sample of Galaxies from the Simulations of Hierarchical Cluster Formation

The sample of galaxies to be re-simulated is chosen from the lower resolution cosmological simulations reported in Paper I. The Particle-Mesh (PM) simulations use constrained initial conditions to produce representative clusters of galaxies for the three cosmological scenarios: $\Omega_0 = 1$ (cluster I), $\Omega_0 = 0.4$ (cluster II), and $\Omega_0 = 0.4, \Omega_\Lambda = 0.6$ (cluster III). All clusters have the same one-dimensional velocity dispersion, 660 km s^{-1} , and mass, $4 \times 10^{14} M_\odot$. The virial radii of the clusters are $\{1.0, 1.5, 1.4\} h^{-1} \text{ Mpc}$, respectively. The Hubble constant is taken to be $H_0 = 65 \text{ km s}^{-1} \text{ Mpc}^{-1}$ ($h = 0.65$). The mass function of identified halos follows the prediction of the Press-Schechter theory for halos more massive than $3 \times 10^{11} M_\odot$ in Cluster I and $\sim 10^{12} M_\odot$ in Clusters II and III. Some of the lower mass halos are missing due to overmerging, because the PM resolution is only $60 h^{-1} \text{ kpc}$. The orbits of 100 most massive galaxies in each cluster are traced through the simulation starting from redshift $z = 5$ using a subset of the most bound galactic particles to calculate its center-of-mass motion.

The galactic trajectories calculated in Paper I are unique among other cosmological simulations in that (i) they are real trajectories of the halos in the evolving cluster, and not equilibrium orbits in the final cluster potential; (ii) the motion of each identified halo is traced through the simulation at each time step with an unprecedented temporal resolution, $\sim 10^7 \text{ yr}$; (iii) the trajectories are calculated only for 1 Hubble time, which limits the average number of orbital periods to 2–4; and (iv) the trajectories are affected by the triaxiality of the cluster halo, which can make initially radial orbits gain angular momentum and avoid the central regions.

The orbital eccentricity of a galaxy is defined as $\varepsilon \equiv (R_a - R_p)/(R_a + R_p)$, where R_a and R_p are the median apo- and pericenter distances, respectively, of the galactic orbit between $z = 5$ and $z = 0$. The median eccentricities for the sample of galaxies in the three clusters are $\varepsilon_{\text{med}} = \{0.27, 0.53, 0.38\}$. They are lower than in the high-resolution simulation of Ghigna et al. (1998), who integrated the orbits in the spherically-symmetric

potential approximating the cluster at the present. The different method of calculating orbits may be the cause of the difference in the results.

In addition to the smaller eccentricities, the physical (not comoving) pericenter distances of galaxies in Cluster I are also larger. For the three cluster samples, $R_{p,\text{med}} = \{560, 160, 290\}$ kpc. The pericenter distances may be relatively large because the clusters move throughout the simulation as they form hierarchically. Since the galaxies are first identified at $z = 5$, the cluster center of mass travels on average 5.2 comoving Mpc. As a result of cluster evolution, the galaxies often pass at a significantly larger distance from the center than they would have in a fixed cluster model.

The resimulated galaxies are chosen from each of the three cluster samples. The galaxies ranked #4 by mass represent large spirals and are denoted {L1,L2,L3} for the cluster models {I,II,III}, respectively. The orbital eccentricities of these galaxies, $\varepsilon = \{0.27, 0.65, 0.38\}$, are typical of their clusters. Two additional spirals, L3a and L3b (ranked #13 and #73), are chosen from the Cluster III sample in order to investigate the variance of the results within a given cosmological model. In comparison with galaxy L3, they have lower eccentricities ($\varepsilon = 0.27$ and 0.09 , respectively) and smaller pericenter distances ($R_p = 220$ and 160 kpc versus $R_p = 230$ kpc for L3).

Three low surface brightness galaxies {LSB1, LSB2, LSB3} are modeled using the same orbit and external tidal field of galaxy L3 but with different masses and sizes. Also, one galaxy from the bottom of each cluster sample represents the dwarf spheroidal galaxies, {D1,D2,D3}. Halos D1 and D2 are ranked #93 by mass, while halo D3 is ranked #87. They all have low eccentricities, $\varepsilon = \{0.06, 0.09, 0.24\}$, and orbit in the outskirts of their clusters.

The initial parameters of the selected models are listed in Table 1. The large galaxies are fairly massive spirals, with the peak of circular velocity at 250 km s^{-1} . The fiducial value of the halo mass, $M_h = 8 \times 10^{11} M_\odot$, is not much lower than the true masses of L1-L3 in the cluster simulations ($\sim 2 \times 10^{12} M_\odot$). The fiducial dwarf model had to be scaled down, because all identified halos in the cluster simulations are relatively massive ($\gtrsim 10^{11} M_\odot$). This would not change the tidal histories of the dwarfs because they are still too small

to affect the evolution of the cluster potential.

4. Numerical Method

The dynamical evolution of galaxies is modeled using the Self-Consistent Field method (Hernquist & Ostriker 1992). In this type of collisionless N -body code, the potential and density are expanded in a series of biorthogonal basis functions

$$\Phi(\mathbf{r}) = \sum A_{nlm} \Phi_{nlm}(\mathbf{r}), \quad (5)$$

$$\rho(\mathbf{r}) = \sum A_{nlm} \rho_{nlm}(\mathbf{r}), \quad (6)$$

which satisfy individually Poisson's equation:

$$\nabla^2 \Phi_{nlm}(\mathbf{r}) = 4\pi G \rho_{nlm}(\mathbf{r}). \quad (7)$$

This assures that the linear combinations of the basis functions satisfy Poisson's equation automatically. The basis functions employed by Hernquist & Ostriker (1992) consist of the ultraspherical polynomials of r and the spherical harmonics $Y_{lm}(\theta, \phi)$. The expansion is truncated at $n_{\text{max}} = 10$ and $l_{\text{max}} = 6$, with m running as usual from $-l$ to l .

The SCF code has been modified for the current problem by Gnedin & Ostriker (1999) and Gnedin, Hernquist & Ostriker (1999). It has been optimized to run on parallel computers and offers an almost ideal scaling with the number of CPU. The simulations were done on the SGI Origin 2000 supercomputer, using 10^6 particles each in the disk and in the halo. The simulation with 2×10^6 particles takes about 20 hours on 16 R10000 processors.

The capability to use a large number of particles in the parallel SCF code offers a high mass resolution of the galactic simulations. The masses of stellar particles in the models of large spirals are $4 \times 10^4 M_\odot$ and in the models of dwarfs only $100 M_\odot$. Halo particles are more massive, however, in proportion to the total halo mass. Also, the simulations gain from the capability to resolve temporal variations of the external tidal field on a scale of 10^7 yr.

All simulations start with a galaxy running in isolation for one rotational period T_{rot} at the half-mass radius of the disk ($R_{1/2} \approx 1.7 R_0$). The particles reach dynamical equilibrium but do not experience yet any appreciable heating. Then the external tidal field is applied for the amount of

time elapsed since $z = 5$ until $z = 0$ in the three cosmological scenarios (T_{sim} in Table 3).

The computations are done in dimensionless units, $G = M_d = R_0 = 1$. Since the components of the tidal tensor $F_{\alpha\beta}$ have dimensions of Gyr^{-2} , they are converted to the internal units using only one parameter, $t_0 \equiv (GM_d/R_0^3)^{-1/2}$. For example, for the models of large spirals the conversion factor is $t_0 = 1.2 \times 10^7$ yr, or about 10% of the rotational period.

4.1. Initial Galactic Models

The initial conditions for the disk galaxy simulations were generated using a set of routines from Hernquist (1993). The stellar disk is a double-exponential, with the density profile

$$\rho_d(R, z) = \frac{M_d}{4\pi R_0^2 z_0} e^{-R/R_0} e^{-|z|/z_0}, \quad (8)$$

where M_d is the disk mass, R_0 is the radial scale length, and z_0 is the vertical scale height. The dark halo is spherically symmetric and corresponds to the isothermal sphere over some radial interval:

$$\rho_h(r) = \frac{M_h}{2\pi^{3/2}} \frac{\alpha}{R_t (r^2 + R_c^2)} e^{-r^2/R_t^2}, \quad (9)$$

where M_h is the halo mass, R_c is the core radius, and R_t is the initial truncation radius. The normalization constant α is

$$\alpha = \left(1 - \sqrt{\pi} q e^{q^2} [1 - \text{erf}(q)]\right)^{-1}, \quad (10)$$

where $q \equiv R_c/R_t$. Halos are effectively truncated at R_t to reduce the computational task of following the orbits of very distant particles. In simulations with the external tidal field, the halos are always stripped to a smaller radius so that the initial choice of R_t is unimportant. For models L1–L3 and D1–D3 I take $R_t = 20 R_c$, and for models LSB1–LSB3 $R_t = 6 R_c$. In all initial models $R_c = R_0$.

Figure 1 shows the disk and halo contributions to the circular velocity

$$V_c(r) = \left(\frac{GM(r)}{r}\right)^{1/2} \quad (11)$$

of the initial models of large spirals. The disk dominates over the inner scale length, R_0 , and the halo

dominates at larger radii. The combined rotation curve is flat out to $10 R_0$.

The figure of the halo is determined using the eigenvalues of the reduced tensor of inertia, $I_{ij} \equiv \int x_i x_j dM$. The particle coordinates are rotated into a new frame where the inertia tensor is diagonal. The axis ratios of the triaxial ellipsoid are calculated as $b/a = (I_{22}/I_{11})^{1/2}$ and $c/a = (I_{33}/I_{11})^{1/2}$, with $c < b < a$. The halos are initially spherical with an isotropic velocity distribution.

The initial orientation of the galactic disk with respect to the coordinate frame of the cluster simulation from Paper I can be set arbitrarily. I assume that the axes of the large galaxies are parallel to the cluster frame and the axes of the dwarf galaxies are tilted by 45° . The tidal tensor has comparable components in all directions, and therefore the results should not depend on the initial disk orientation.

4.2. Tests in Isolation

Before studying the effects of tidal heating, it is very important to assess the extent to which the simulations are affected by numerical artifacts. The main is numerical relaxation, which results in erroneous heating of stellar orbits. This relaxation arises from Poisson fluctuations of the coarse-grained potential represented by a finite number of particles, $N \sim 10^6$. This is much smaller than the number of stars in real galaxies, and therefore the relaxation rate is artificially high (e.g. Weinberg 1996).

I have run five test models in isolation in order to check the dependence of numerical heating on the number of particles and the time step (Tables 2a and 2b). The first model, L–isol, is the main model for large spiral galaxies L1–L3 and the next three are its modifications with reduced number of particles or increased time step. The last isolated model, LSB–isol3, is that of a large low surface brightness galaxy LSB3. The tests run for 12 Gyr, the longest simulation time of the three cosmological scenarios.

Due to the diffusive nature of the relaxation process, both the first and second order changes of stellar energy are comparable, $\langle \Delta E/E \rangle \sim \langle (\Delta E/E)^2 \rangle$. However, the former may change sign and vary randomly, whereas the latter rises

monotonically in time and offers a better measure of relaxation. The average energy change of disk particles at the end of run L–isol is small, $\langle(\Delta E/E)^2\rangle \approx 0.5\%$. Table 2a shows that the radial mass distribution of the disk remains exponential and the scale length, R_0 , changes only by 4%. The halo also remains spherical, with the axis ratios b/a and c/a close to unity. The only noticeable difference is the vertical heating of the disk. The average scale height, z_0 , increases by a factor 1.7 and the vertical velocity dispersion σ_z^2 rises similarly. As Figure 6 shows (lower dots), the thickening is stronger near the center where the density of particles is higher and the relaxation is expected to be faster.

Another statistic of disk heating is the change of the linear vertical energy. In equilibrium it can be defined using the epicycle theory as

$$E_z = \frac{v_z^2}{2} + \frac{1}{2} \left(\frac{\partial^2 \Phi}{\partial z^2} \right)_0 z^2, \quad (12)$$

where the second derivative of the potential is evaluated in the plane of the disk (for a thin disk it is $2\pi G\Sigma(R)/z_0$, where $\Sigma(R)$ is the surface density). Equation (12) is strictly an integral of motion only near the midplane, where the disk dominates gravity. In the isolated runs the vertical energy E_z changes significantly more than the total energy E , by the order itself (Table 2b). But this is consistent with the changes of the scale height and the vertical velocity dispersion.

With half the number of particles in model L–isol2, the second order energy change is 0.8%. The vertical energy and the scale height are proportionately larger, while the radial scale length and the figure of the halo are unchanged. If only the number of disk particles is reduced (model L–isol3), the heating is slightly less but similar to the previous case. Thus only the vertical structure of the disk is sensitive to numerical relaxation, when the number of particles in simulation $N \sim 10^6$.

The time step in the main simulations is $\Delta t = 0.1 t_0$ in code units, or about 1% of the half-mass rotation period, $T_{\text{rot}} \equiv 2\pi R_{1/2}/V_c$. In a thin disk the stellar orbits should be calculated accurately even in the center, where the rotation period decreases by 60% as the disk density increases by a factor of 5. However, once the relaxation raises velocities artificially high, the stellar motion deviates more and more significantly from the original

orbits. Doubling the time step in model L–isol1 leads to larger energy changes than in the other isolated models. This effect is coupled to numerical relaxation and, therefore, both are more important in the inner parts of the galaxy. This is not a problem for the present study because, by construction, external tidal forces vanish in the center. Tidal effects are more significant in the outer regions of the galaxy where both numerical artifacts are less important.

While the artificial thickening of the disk is certainly undesirable, it can be corrected for in a statistical way. The relaxation rate, $d\langle(\Delta E/E)^2\rangle/dt$, is constant in time and the scale height $z_{0,\text{num}}$ increases linearly (cf. upper panel of Figure 10), as expected for pure Poisson fluctuations. Thus at any time it can be subtracted from the real simulation to accentuate the effects of tidal heating. Assuming that the numerical heating is statistically independent from the external tidal heating, the two effects add in quadrature and the modified scale height can be defined as

$$\bar{z}_0 \equiv (z_0^2 - z_{0,\text{num}}^2 + z_{0,i}^2)^{1/2}, \quad (13)$$

where $z_{0,i}$ is the initial scale height. The least squares fit to the growth rate is

$$d \ln z_{0,\text{num}}/dt = (6.0 \pm 0.05) \times 10^{-2} \text{ Gyr}^{-1}. \quad (14)$$

In the following section we derive the rate of numerical relaxation in a thin disk to confirm that the growth of $z_{0,\text{num}}(t)$ is consistent with the self-interaction of disk particles and with the heating by more massive halo particles.

4.3. Numerical Relaxation in a Thin Disk

Spitzer & Hart (1971) have derived the median relaxation time for a smooth spherical system of mass M and half-mass radius R_h :

$$t_{rh} = 0.14 \frac{N}{\ln \Lambda} \left(\frac{R_h^3}{GM} \right)^{1/2}. \quad (15)$$

It describes very well the rate of heating in simulations, even including the resonant interactions of stars (see the discussion in Gnedin & Zhao 2002, based on the results of Weinberg 1993). The relaxation is dominated by distant encounters with large impact parameters b_{\max} , parametrized by the Coulomb logarithm, $\ln \Lambda = \ln b_{\max}/b_{\min}$. The system relaxes on many ($\sim 0.1N$) dynamical times and for large enough N can be considered collisionless.

However, Rybicki (1971) has emphasized that the relaxation time is much shorter in the infinitely thin disks, of the order an orbital period (see also Binney & Tremaine 1987, problem 8-6). This is due to the close encounters dominating in 2D geometry, instead of the distant encounters in 3D geometry. In a disk of finite thickness this effect largely disappears, but there is another effect that leads to faster relaxation. The collective response of stars to a perturbation is greatly enhanced when the stellar motions are highly ordered in a kinematically cold disk (Sellwood 1987). Since the stellar orbits are still largely confined to a plane, the most noticeable effect of disk relaxation is the heating in vertical direction.

4.3.1. Heating by Disk Particles

For the general case of a thin disk with an initial scale height $z_{0,i} \ll R_0$ and vertical velocity dispersion $\sigma_{z,i} \ll V_c$, the relaxation rate can be estimated as follows. The velocity kick in the vertical direction from a single encounter with a star m_* at an impact parameter b and relative velocity v is $\Delta v_z \approx 2Gm_*/vb$. The encounter velocity is of the order the radial and azimuthal dispersion in the plane. Most of stellar encounters take place at a median height above the plane, where the density of the double-exponential disk (eq. [8]) is half of that in the plane, $\rho_d(R, z_{1/2}) = 1/2 \times \Sigma(R)/2z_0$. The integrated effect of encounters at all impact parameters is then

$$\frac{d\sigma_z^2}{dt} = \int_{b_{\min}}^{b_{\max}} \left(\frac{2Gm_*}{vb} \right)^2 \frac{\Sigma(R)}{4z_0 m_*} v 2\pi b db = \frac{2\pi G^2 m_* \Sigma(R) \ln \Lambda_d}{v z_0(t)}, \quad (16)$$

where $b_{\max} \sim 2z_0 \sim 0.6$ kpc and $b_{\min} \sim 0.1$ kpc (set by the resolution scale). In the simplest case, as a result of heating the surface density $\Sigma(R)$ remains the same but the scale height z_0 increases in time. The rate of increase can be calculated from the relation $\sigma_z^2 = \pi G \Sigma(R) z_0$, which should hold as long as the disk is still relatively thin:

$$\frac{dz_0}{dt} = \frac{1}{\pi G \Sigma(R)} \frac{d\sigma_z^2}{dt} = \frac{2Gm_* \ln \Lambda_d}{v z_0}. \quad (17)$$

The solution is

$$\frac{z_0}{z_{0,i}} = \left(1 + \frac{2t}{t_{\text{rel},z}} \right)^{1/2}, \quad (18)$$

where the vertical relaxation time is

$$t_{\text{rel},z} = \frac{N_d}{2 \ln \Lambda_d} \frac{v z_{0,i}^2}{GM_d} = 11 N_{d,6} \text{ Gyr} \quad (19)$$

for $v = 80 \text{ km s}^{-1}$, $M_d \equiv N_d m_* = 4 \times 10^{10} M_\odot$, $z_{0,i} = 0.3$ kpc, $\ln \Lambda_d = 1.8$, and $N_{d,6} \equiv N_d/10^6$. The corresponding rise of the vertical velocity dispersion is

$$\frac{\sigma_z}{\sigma_{z,i}} = \left(\frac{z_0}{z_{0,i}} \right)^{1/2} = \left(1 + \frac{2t}{t_{\text{rel},z}} \right)^{1/4}. \quad (20)$$

This matches qualitatively the heating of the disk by massive molecular clouds (cf. Lacey 1984). The initial growth is linear and the maximum rate is $d \ln z_0 / dt = t_{\text{rel},z}^{-1} \approx 9 \times 10^{-2} \text{ Gyr}^{-1}$, which is in reasonable agreement with the observed rate of growth in the isolated simulation (eq. [14]).

If the stars were distributed spherically rather than in the disk, the relaxation time would be significantly longer (eq. [15]), $t_{rh} \approx 10^{12} \text{ yr}$. Alternatively, if the stars were confined to an infinitely thin disk, the heating rate (in the plane) would be

$$\frac{d\sigma_R^2}{dt} = \int_{b_{\min}}^{b_{\max}} \left(\frac{2Gm_*}{vb} \right)^2 \frac{\Sigma(R)}{m_*} v 2db \approx \frac{8G^2 m_* \Sigma(R)}{vb_{\min}}. \quad (21)$$

This rate (clearly dominated by close encounters) is faster than the finite-thickness rate (dominated by distant encounters, eq. [16]) by a factor $2.1 z_0(t)/z_{0,i}$. So as expected, the finite-thickness disk provides an intermediate case between the 2D and the 3D geometry.

4.3.2. Heating by Halo Particles

When the disk is surrounded by a dark halo, the heating by massive halo particles can be more important. The heating rate by the particles with mass m_h and density ρ_h is

$$\frac{d\sigma_z^2}{dt} = \int_{b_{\min}}^{b_{\max}} \left(\frac{2Gm_h}{vb} \right)^2 \frac{\rho_h}{m_h} v 2\pi b db = \frac{8\pi G^2 m_h \rho_h \ln \Lambda_h}{v}, \quad (22)$$

where the encounter velocity v is dominated by the halo dispersion, σ_h . The ratio of the heating rates due to the halo and disk particles is

$$\frac{(d\sigma_z^2/dt)_h}{(d\sigma_z^2/dt)_d} = \frac{m_h \rho_h \ln \Lambda_h v_{\text{enc},d}}{m_* \rho_d \ln \Lambda_d v_{\text{enc},h}}. \quad (23)$$

The typical parameters in our models at R_0 are $m_h/m_* = 20$, $v_{\text{enc},h}/v_{\text{enc},d} \approx 2$, and $\rho_d/\rho_h \approx 5 - 10$, so the two heating rates are comparable. However, the growth of the scale height is different because now the right-hand side of equation (22) is independent of σ_z and

$$\frac{z_0}{z_{0,i}} = \left(\frac{\sigma_z}{\sigma_{z,i}} \right)^2 = 1 + \frac{t}{t_{\text{rel},h}} \quad (24)$$

with

$$t_{\text{rel},h} = \frac{N_h}{8\pi \ln \Lambda_h} \frac{\sigma_{z,i}^2 v}{G^2 M_h \rho_h}. \quad (25)$$

This interaction with the halo particles is equivalent to the heating by massive black holes (cf. Lacey & Ostriker 1985). For $M_h = 8 \times 10^{11} M_\odot$, $v \approx 160 \text{ km s}^{-1}$, $\sigma_{z,i} \approx 80 \text{ km s}^{-1}$, $\ln \Lambda_h \approx 2$, and $\rho_h(R_c) \approx 0.08 M_\odot \text{ pc}^{-3}$, the relaxation time is $t_{\text{rel},h} \approx 17 N_{h,6} \text{ Gyr}$. This is in excellent agreement with the growth rate in the isolated simulation (eq. [14]). Thus, both disk and halo particles contribute to the disk thickening, although in the long run the heating by halo particles would dominate.

Having a certain understanding of the numerical relaxation in the disk, when it sets in (eqs. [19] and [25]) and how to account for it (eq. [13]), we move to the simulation results.

5. The Transformation of Large Spiral Galaxies

We start with the results for large disk galaxies. Figure 2 shows the distribution of particles at the beginning and the end of the simulation of galaxy L1. The first important result is that the galaxy survives tidal heating. It still looks like a disk galaxy of roughly the same size. Large, coherent spiral arms form in the outer regions. The disk shrinks in the radial direction and flares at the fuzzy edges. But the main difference from the initial configuration is a substantial thickening of the disk. Viewed at a certain surface brightness limit, this thick and round disk galaxy may be classified as an S0.

The dark matter distribution is relatively simple. The galaxy has been stripped of about 40% of its halo (Table 3) and has shrunk to the limits of the stellar disk. Inside the truncation radius, the halo has been little affected (Figure 3). The figure of the halo becomes triaxial but only mildly, with the smallest axis ratio $c/a = 0.88$. Thus, the amount of the remaining halo mass is indicated simply by the truncation radius, R_t . For galaxy L1 it changes from 60 kpc to 37 kpc. Figure 4 shows that the rotation curve is still flat up to six disk scale lengths. The circular velocity, measured at $5R_0$, is decreased only by 2%.

The disk of the galaxy is perturbed more significantly. Figure 5 shows that the surface density decreases in the center but increases between $3R_0$ and $4R_0$, relative to the initial profile. The surface density exhibits noticeable wiggles superimposed on the otherwise exponential disk.

In addition to truncating the halo, a major effect of tidal heating is the thickening of the disk. By construction, the external tidal force vanishes at the center and increases linearly with radius. Figure 6 demonstrates that the disk flares in the outer parts. Numerical relaxation affects the disk structure only within the inner two scale lengths, where tidal heating is negligible. At $R > 2R_0$, the external tidal effects are clearly dominant.

A direct evidence of tidal heating is the dramatic increase of all three velocity components in the outer regions of the disk (Figure 7). The velocity dispersion increases at the expense of the rotation speed, which starts to decline at around four scale lengths from the center (while the circu-

lar velocity is still flat; cf. Figure 4). In contrast, the velocity dispersion of the halo decreases in the outer parts due to the significant mass loss.

The analysis of the other large spirals shows a lot of similarity but with quantitative differences. Since the tidal field is stronger in the low Ω_0 clusters (see §5.3), galaxies L2 and L3 are subject to stronger perturbations than galaxy L1. Galaxy L2 suffers the biggest mass loss, about 64%, while galaxy L3 provides the intermediate case with about 50%. Their truncation radii fall below 30 kpc. The disks of both galaxies L2 and L3 are heated more strongly than in galaxy L1.

Figure 8 shows that the mass loss from the three halos is not steady. There are several instants of large losses associated with the maxima of the tidal force. Examining the particle distribution at successive epochs reveals how the halo is being stripped. After a strong tidal shock, a cloud of dark matter particles disperses across the tidal boundary and slowly drifts away from the galaxy in two opposite directions along the same line. That line corresponds to the direction of the strongest component of the tidal tensor at the time. The unbound particles are later stretched along that direction further and further away from the galaxy.

As Figure 9 shows, the disk scale lengths of all three galaxies remain almost constant. In contrast, the vertical scale heights rise monotonically with time (Figure 10). While a part of this effect is due to the numerical relaxation (eq. [13]), the corrected scale height \bar{z}_0 measures the thickening only due to the tidal heating. Galaxy L2 leads in the rate of expansion, in agreement with other indicators of evolution, the mass loss and the velocity dispersion increase. At the end of the run, its scale height is more than doubled. The other two galaxies experience more modest evolution. In particular, the disk of galaxy L3 had expanded to its maximum height in 7 Gyr and then remained effectively unchanged for the same amount of time until the present.

5.1. Dependence on Time Step and Number of Particles

In order to quantify the dependence of the results on numerical details, such as the time step and the number of particles, I have run three ad-

ditional models of galaxy L3 (Table 4). They are simulated using the same parameters as the isolated models {L-isol1, L-isol2, L-isol3} but with the external tidal field of galaxy L3. The corresponding isolated runs are used to correct the scale height \bar{z}_0 .

In model 1, the time step is doubled while the number of particles is kept the same, relative to the main model of L3. As discussed in §4.2, the time step is chosen small enough to represent accurately stellar orbits even in the center; $\Delta t = 0.01 T_{\text{rot}} \approx 10^6$ yr. Indeed, with the doubled time step model 1 reproduces most of the features of model L3. The main changes are the 13% stronger thickening of the disk and a slightly longer radial scale length.

In model 2, half the number of particles is used in both the disk and the halo with the original time step. The results are very close to those of model L3. The changes of the scale length and the corrected scale height are not noticeable at all.

In model 3, where only the number of disk particles is reduced by half, the scale height grows even less than in model L3. This indicates that most of the numerical heating of disk particles is produced by the interaction with massive halo particles, as expected. In all three test runs the halo structure and mass loss are virtually identical.

The conclusion from these tests is that only the vertical structure of the disk is sensitive to numerical effects. Variations of the time step and the number of particles affect the corrected scale height \bar{z}_0 by 10% to 30%. Thus the deviation of our main results from the case of infinite resolution is expected to be of the same order.

5.2. Dependence on Force Resolution

The necessary truncation of the spherical harmonics series in equation (5) imposes a limit on the vertical force resolution in a thin disk. An accurate calculation of the force with $z_0/R_0 = 0.1$ may require the expansion order $l_{\text{max}} \sim 100$. Our simulations with $l_{\text{max}} = 6$ thus have an effectively smoothed vertical force within the disk, and the comparison with the forces calculated by direct summation shows significant deviations at $|z| \lesssim 0.4 R_0$. From the SCF simulations alone it is difficult to assess how this could affect the response of the disk to external perturbations. In or-

der to test sensitivity of the results to force resolution, I use the publicly-available tree code GADGET (Springel, Yoshida & White 2001) and resimulate large galaxy models L1, L2, and L3.

The tree algorithm with an accuracy parameter $\theta = 0.8$ calculates the vertical forces in our thin disks within 1% of the direct summation result. The algorithm is, however, much more computationally expensive and can be realistically used only with a subset of particles. With $N_d = 10^5$, $N_h = 4 \times 10^5$, one parallel GADGET simulation takes 150 hours on 8 processors of the beowulf PC cluster at STScI. I use a 'type 0' time step criterion based on local particle acceleration a and softening parameter ϵ : $\Delta t \propto \sqrt{\epsilon/a}$, and limit the time step not to exceed 0.1 in code units ($\approx 10^6$ yr, the same step as in the SCF runs). The average time step was 0.04 – 0.08 in code units. In order to adequately resolve the vertical structure of the disk and to minimize relaxation effects, I take the softening parameter $\epsilon_d = 0.1z_0$ for disk particles and $\epsilon_h = 0.1R_0$ for halo particles, using the definition of Springel, Yoshida & White (2001).

Since the numerical heating of the disk is largely due to the massive halo particles, I run two sets of models increasing N_h from 10^5 to 4×10^5 . The number of disk particles is fixed at $N_d = 10^5$ (these numbers are limited by a realistic run time). In the control run in isolation with $N_h = 10^5$ the disk size shows a large increase ($z_0/z_{0,i} = 3.0$) but so does a corresponding SCF run with the same number of particles ($z_0/z_{0,i} = 3.1$). In the control run with $N_h = 4 \times 10^5$ the numerical heating is already reduced ($z_0/z_{0,i} = 1.9$) almost to the level of the main SCF runs. In both isolated GADGET simulations the radial scale length changes by less than 1%. This agrees with the discussion in §4.3 that numerical heating depends primarily on the number and masses of particles.

Table 5 shows the results of GADGET simulations for models L1–L3. Overall, the disk heating is somewhat stronger than in the SCF runs: both \bar{z}_0 and R_0 increase by roughly 10%. The vertical heating is much stronger in the runs with fewer halo particles – this is clear evidence that numerical relaxation can affect the evolution of thin disks even with adequate force resolution.

The thickening of the disk is less monotonic in the GADGET runs. Sudden jumps of \bar{z}_0 , for example at 5 Gyr and 9 Gyr for model L2, coincide with

larger than usual deviations of the disk center-of-mass from the halo center-of-mass. The two can differ by $\Delta R_{CoM} \lesssim 800$ pc after a strong perturbation, and in such an unrelaxed state the disk appears thicker. Note that this deviation is still within $0.3 R_0$. In models L1 and L3, and in all SCF runs, $\Delta R_{CoM} < 100 - 200$ pc.

The disk appears symmetric in the vertical direction and shows no sign of warping. The orientations of the inner and outer parts of the disk, divided at $2.5 R_0$, differ by less than 5° (8° for SCF runs).

A noticeable difference in the GADGET runs is the radial expansion of the disks. In the SCF models, R_0 was essentially unchanged. This might be a result of the restoring forces being effectively “anisotropic” within the disk: while the radial expansion is sufficiently accurate, the vertical expansion is smoothed. Fortunately, the difference with the GADGET results is only 10 – 15%.

As a result of the increase of R_0 , the circular velocity drops correspondingly by about 10% in all GADGET models. However, the halo structure in the GADGET runs almost exactly mirrors that in the SCF runs. The only deviation of the halo mass is in model L3 (by 3%), while the shapes of the halos are similar. I conclude that apart from R_0 , the only quantity susceptible to the errors in force resolution is \bar{z}_0 , and while it increases by a factor 1.6 – 2.4 in the SCF runs the true value is probably in the range 2 – 3.

5.3. Dependence on Tidal History

In cluster simulations presented in Paper I, the amount of tidal heating has been estimated using the tidal heating parameter, I_{tid} . It is simply the square of the integrated velocity change summed over all peaks of the tidal force $F_{\alpha\beta}$ ($\alpha, \beta = \{x, y, z\}$):

$$I_{\text{tid}} \equiv \sum_n \sum_{\alpha, \beta} \left(\int F_{\alpha\beta} dt \right)_n^2 \left(1 + \frac{\tau_n^2}{t_{\text{dyn}}^2} \right)^{-3/2}. \quad (26)$$

It is also corrected for the conservation of adiabatic invariants of stellar orbits when the external perturbations are long, using the parametrization of Gnedin & Ostriker (1999). Here τ_n is the effective duration of peak n for each value of α and β , and t_{dyn} is the half-mass dynamical time of the

galaxy ($\sim T_{\text{rot}}$). The average energy change due to tidal heating for the stars at radius r is

$$\langle \Delta E \rangle = \frac{1}{6} I_{\text{tid}} \langle r^2 \rangle. \quad (27)$$

This semi-analytical estimate provides a good description of the energy changes of particles in the simulation and can be used to compare tidal effects for different galaxies.

The galaxies in each cluster sample show an exponential distribution of the tidal parameter, $N(I_{\text{tid}}) = N_0 \exp(-I_{\text{tid}}/I_0)$. The characteristic parameter I_0 is the largest in Cluster II ($5 \times 10^3 \text{ Gyr}^{-2}$), intermediate in Cluster III ($2 \times 10^3 \text{ Gyr}^{-2}$), and the smallest in Cluster I ($8 \times 10^2 \text{ Gyr}^{-2}$; see Paper I). The simulations of galaxies L1–L3 show noticeable differences in the evolution of large spiral galaxies in the three cosmological models. In agreement with the estimates of the tidal heating parameter, galaxy L2 experiences stronger evolution than galaxies L1 and L3.

However, these differences may not serve as a clear discriminant among the cosmological models. The distribution of tidal parameters within the same cluster leads to a comparable variance of the results. The additional simulations of two galaxies from Cluster III prove this point.

The two computed models, L3a and L3b, use the same initial conditions as galaxy L3 but different tidal histories. These galaxies, corresponding to the Cluster III halos #13 and #73, have some of the largest heating parameters, $I_{\text{tid}} = 3.8 \times 10^3 \text{ Gyr}^{-2}$ and $I_{\text{tid}} = 6.4 \times 10^3 \text{ Gyr}^{-2}$, respectively. For comparison, the reference galaxy L3 has $I_{\text{tid}} = 4.2 \times 10^3 \text{ Gyr}^{-2}$. These models represent the strongest cases of tidal evolution.

As expected, galaxy L3b loses more mass and develops a thicker disk than model L3, while for L3a the trend is the opposite (Table 3). The final state of galaxy L3b is similar to that of model L2 from Cluster II. On the other hand, galaxy L3a is closer to model L1 from Cluster I. Thus the distribution of tidal histories of galaxies within the same cluster leads to a similar variation of the dynamical evolution.

The adiabatic correction factor in equation (26) is very important. It accounts for the temporal structure of the tidal field and suppresses the perturbations with long timescales to which galaxies respond adiabatically. Without that factor,

galaxy L3a would have had a higher value of I_{tid} than galaxy L3b. The difference is due to the tidal force being more “impulsive” for galaxy L3b, while being more “adiabatic” for L3a.

5.4. Do spirals become S0 galaxies?

The simulations of large spiral galaxies show that the kinematic heating and vertical expansion of the disks lead to a significant morphological transformation. An initially normal spiral may be identified in the end as a lenticular galaxy, an S0. The following section puts this claim to a thorough observational check.

The final snapshot of galaxy L1 (Figure 2) looks similar to the deep exposures of the S0 galaxy NGC 4762 (Sandage 1961; Burstein 1979). The disk is thick and ends with fuzzy warps. A modest central mass concentration is seen in both the simulation and the real galaxy.

The most detailed data are available for nearby S0 galaxies in the field (Kent 1985). The HST images of lenticulars in distant clusters (Ellis et al. 1997; van Dokkum et al. 1998) usually provide only integrated light and colors. Typically, the surface brightness profiles of S0s are well fitted by a combination of the exponential disk and the $r^{1/4}$ bulge. The simulations reported here do not include a bulge component initially. In fact, one of the goals of this study was to investigate whether a bulge forms as a result of tidal heating. Two competing effects play a role here: stars on average gain energy from tidal perturbations and move generally outward; on the other hand, the tidally-induced energy dispersion contributes to two-body relaxation and accretion onto the center. Figure 5 shows that no appreciable bulge forms from the disk particles, asserting that the relaxation time is still much longer than the age of the galaxy. However, the interstellar gas may be driven inward by tidal effects and ignite a burst of star formation (Hernquist & Mihos 1995; see also §5.5). This would assist in the formation of a prominent bulge.

S0 galaxies typically have the same disk scale lengths as the spirals of similar luminosity (Kent 1985). In the present simulations the scale length R_0 is virtually unchanged. Also, the axis ratios of the simulated disks, 0.15 to 0.25, are consistent with the average observed value of 0.2-0.25

for the “thick disks” (Binney & Merrifield 1998). Burstein (1979) attempted to decompose the vertical brightness profile of late type edge-on galaxies into a combination of the thin and thick disks. The latter dominate in the outer regions of the galaxies and are much more prominent in S0s than in spirals. Thick disks are not as centrally peaked as thin disks and have a shallow radial gradient: they look “diffuse” and “boxy”. All this is consistent with having a tidal origin; flaring of the disk was expected and has been detected in the simulations.

Kinematic information is available only for the local galaxies. In a cold exponential disk, vertical velocity dispersion should fall with radius as the surface density: $\sigma_z^2(R) = 2\pi G z_0 \Sigma_0 \exp(-R/R_0)$. In a sample of ten S0 galaxies (Seifert & Scorza 1996) the velocity dispersion flattens at 50 – 100 km s^{-1} and even rises in the outer regions. Similarly, a large study of the early type galaxies by Simien & Prugniel (1998) shows a systematic increase of the total velocity dispersion at large radii, often exceeding 100 km s^{-1} . Present simulations certainly confirm this trend.

Finally, note that bars are commonly found in S0 galaxies. A single tidal interaction may excite bar instability in an axisymmetric galaxy, but a succession of tidal shocks and the resulting kinematic heating would isotropize stellar orbits and destroy the bar. The actual survival of bars, then, depends on the amount of tidal heating in the inner galaxy (see Sellwood 1999). Present simulations, which include a stabilizing dark matter halo, do not show any detectable bar.

5.5. Gas Dynamics and Star Formation

The evolution of spiral galaxies depends sensitively on the amount and distribution of the interstellar gas. Even though the collisionless simulations do not address gas dynamics directly, it is possible to infer qualitative features of the gas response to tidal heating.

The external tidal force is not steady in time, it comes in a series of peaks (cf. Figures 14–16 in Paper I). The timescale of each tidal perturbation is of the order 10^8 yr or longer. While the stars would continue to gain energy without dissipation, the gas should cool to its equilibrium temperature fairly quickly. The cooling time of the ionized gas

is

$$t_{\text{cool}} = \frac{\frac{3}{2}nkT}{n_e^2 \Lambda(T)} \approx 7 \times 10^5 \frac{T_6}{n_e \Lambda_{-23}} \text{ yr}, \quad (28)$$

where $\Lambda(T) \sim 10^{-23} \text{ erg cm}^3 \text{ s}^{-1}$ is the cooling function at the temperatures $T \sim 10^6 \text{ K}$, and n and n_e are the baryon and electron number densities, respectively. As a case of extremely fast tidal heating, consider that the gas with $nT \sim 10^4 \text{ K cm}^{-3}$ heats up to $8 \times 10^5 \text{ K}$, corresponding to the velocity dispersion of 100 km s^{-1} . Even in this case, it would cool back to 10^4 K in $4 \times 10^7 \text{ yr}$. In reality the gas would likely heat less efficiently and therefore cool faster.

However, the thick stellar disk is now stable against gravitational perturbations and is unlikely to form new stars. Figure 11 shows Toomre's Q parameter (Toomre 1964) for the final states of galaxies L1–L3. Even the minimum value, $Q_{\text{min}} \approx 2$, is large enough to suppress any axisymmetric disk instability. Under such conditions spiral structure and gaseous shocks would not form in the inner regions of the galaxies. The spiral arms visible in Figure 2 are prominent only in the outer regions, where the diffuse gas is likely to be ionized or stripped by the intracluster medium.

The stability of stellar disks is modified in the presence of cold gas. The low velocity dispersion of the gas amplifies the growth of perturbations and lowers the effective value of Q compared to the pure stellar case. Jog & Solomon (1984) derive a stability criterion for a two-fluid system of the stars and gas. From their equation (22) it follows that the system is unstable if the modified parameter Q_{eff} is less than unity:

$$Q_{\text{eff}} = Q \frac{3.36}{2\pi} \left(\frac{x}{x^2 + 1} + \frac{\beta x}{x^2 + c} \right)^{-1} < 1, \quad (29)$$

where $\beta = \Sigma_{\text{gas}}/\Sigma_*$ is the ratio of the gas to stellar surface densities, $c = v_{\text{th}}/\sigma_*$ is the ratio of the gas thermal velocity to the stellar velocity dispersion, and $x = \kappa/(\sigma_* k)$ is the ratio of the perturbation wavelength, $2\pi/k$, to the effective scale of stellar motion. Here

$$\kappa \equiv \left(\frac{1}{R} \frac{dV_c^2}{dR} + 2 \frac{V_c^2}{R^2} \right)^{1/2} \quad (30)$$

is the epicyclic frequency, which includes the contributions from both stars and dark matter. Equation (29) allows one to determine the amount of

gas, β , required to make the disk unstable. Writing the velocity dispersions as $v_{\text{th}} = 11 T_4^{1/2} \text{ km s}^{-1}$ and $\sigma_* = 100 \sigma_{*,100} \text{ km s}^{-1}$, I find $c = 0.11 T_4^{1/2} \sigma_{*,100}^{-1}$. The most unstable mode is usually a half of the maximum allowed wavelength (Binney & Tremaine 1987), which in this case is $x_{\text{max}} \approx 1.87(1 + \beta)/Q$. With these parameters, the equation $Q_{\text{eff}} = 1$ can be solved numerically to yield $\beta \approx 0.52$. It shows that the disk is unstable only when the mass of cold gas is at least 50% of the stellar mass, a condition rarely satisfied in any spiral or S0 galaxy even in the field.

Current theories of star formation in normal spiral galaxies often rely on a continuous infall of cold gas (e.g., Edvardsson et al. 1993; Dalcanton et al. 1997b). This infall supplies the material for new stars and also helps to sustain a marginal dynamical instability of the disk. After galaxies enter the cluster, external tidal forces halt the late infall and, with it, new star formation.

5.6. Ram Pressure Stripping

The amount of gas remaining in the galaxies can also be reduced by a variety of processes. The intracluster media (ICM) can sweep the diffuse gas via ram pressure (Gunn & Gott 1972). Assuming the ICM density in the cluster core $n_{\text{icm}} = 10^{-3} \text{ cm}^{-3}$ (Jones & Forman 1984), the surface density of H I gas $\Sigma_{\text{gas}} = 4 M_{\odot} \text{ pc}^{-2}$ (Binney & Merrifield 1998), and the orbital velocity of 800 km s^{-1} , large spirals with exponential disks would be stripped of atomic gas down to $R = 5 \text{ kpc}$. Recent numerical simulations of ram pressure stripping in rich clusters (Abadi, Moore & Bower 1999) confirm that the H I disks are truncated at $\sim 4 \text{ kpc}$. Through viscous coupling even the inner gas may be affected (Quilis, Moore & Bower 2000).

The efficiency of ram pressure stripping depends also on the hierarchical formation of the cluster. When individual groups of galaxies merge into the cluster, a bow shock may form slightly ahead of the group's motion. It happens when the ram pressure on the infalling gas increases faster than a sound wave can propagate across the substructure (Fabian & Daines 1991). Numerical simulations (Roettiger, Loken & Burns 1997) confirm that bow shocks do form around the substructures falling in at supersonic speeds. These shocks may delay the heating of gas to the virial temperature.

X-ray observations of the central region of Coma cluster by *ASCA* (Hank Donnelly et al. 1999) find a cold and a hot spots in the temperature map. A natural explanation would be a bow shock associated with the group around the bright galaxy NGC 4869.

While ram pressure stripping does not affect directly dense molecular clouds, the interpenetrating galactic encounters may remove the molecular component (Kritsuk 1983). Direct collisions between molecular clouds would be rare but the coupling via magnetic fields would ensure dynamical interaction. In high-speed collisions the gas would shock and decelerate, whereas the stars and dark matter fly away.

In a survey of 17 bright spirals in the Virgo cluster, Cayatte et al. (1994) find two groups of galaxies with different H I properties. One group has a typical H I surface density ($\sim 4 M_{\odot} \text{pc}^{-2}$) in the inner regions, but a steeply falling one beyond a half of the optical radius. These galaxies could be affected by ram pressure stripping. The other group has lower central surface densities but the gas extends much further, often beyond the optical radius. In other words, the latter galaxies are modestly deficient of H I at all radii, independently of the local gravitational force. Other evaporation mechanisms may play a role here, such as the turbulent mixing or heat conduction (see Sarazin 1988 for details).

Also, in a study of three rich Abell clusters and the Virgo cluster, Valluri & Jog (1991) find that the H I deficiency is stronger in larger spirals. This statistical trend is opposite to that expected for ram pressure stripping, since more massive galaxies should hold on to their gaseous component better. Having considered several possible mechanisms, Valluri & Jog (1991) conclude that the H I deficiency can only be explained by tidal interactions.

Finally, note that numerical simulations of galaxy interactions (Hernquist & Mihos 1995; Barnes & Hernquist 1996) often show a dramatic loss of angular momentum of the gas, drawing it to the center and igniting a powerful starburst. This is corroborated by the observation that galaxies with distorted profiles are more likely to be detected in H α than the undistorted ones (Kennicutt 1998). Moss & Whittle (1993) find a 50% higher detection rate of Sa galaxies in the eight nearby

Abell clusters than in the field. These starbursts may also blow away the remaining gas from small galaxies (Dekel & Silk 1986), leaving behind only compact stellar spheroids.

6. The Disruption of Low Density Galaxies

6.1. Dwarf Spheroidal Galaxies

Dwarf galaxies are abundant in the Universe and dominate the number counts both in the field and in clusters (Ferguson & Binggeli 1994; Gallagher & Wyse 1994). While in the field they are usually found around large luminous galaxies, their distribution in clusters is dramatically different. There are many fewer dwarfs in the center than on the periphery (Phillipps et al. 1998) and there is a strong anti-correlation of the ratio of dwarfs to giants with the local projected density of galaxies (Driver, Couch & Phillipps 1998). Also, less massive clusters are likely to have more dwarf galaxies than large virialized clusters. Observational evidence suggests that dwarfs are subject to strong selection effects in clusters, consistent with tidal disruption.

Dwarf galaxies are usually divided into two distinct classes, the high density dE and the low surface brightness dSph (Kormendy 1985). It is the dark matter-dominated dwarf spheroidals that are likely to be disrupted. For the purpose of this simulation I assume that initially they were disk galaxies embedded in dark matter halos. The surface brightness profiles of many dSph are fairly good exponentials, which supports their disk origin. The typical scale length is about 1 kpc (Ferguson & Binggeli 1994), similar to dwarf irregulars like the LMC (de Vaucouleurs & Freeman 1972). The velocity dispersion of dSph is very low, typically 10 km s^{-1} and no more than 20 km s^{-1} (Kormendy 1985). I assume the latter extreme value to investigate whether even the densest dwarf spheroidals could survive tidal heating.

I run three dwarf models {D1, D2, D3} with the tidal histories from different cluster simulations (see §3). Table 1 shows that the stellar disks are small and are completely dominated by dark matter. Still, the density of the halo cores is low, $\rho_{h,av} \approx 5 \times 10^{-3} M_{\odot} \text{pc}^{-3}$, dangerously close to the critical tidal density (eq. [1]). The peaks of the tidal force can reach as high as 200 Gyr^{-2} , which

corresponds to the tidal density of $3.6 \times 10^{-3} M_{\odot} \text{pc}^{-3}$.

None of the dwarfs survives until the end of the simulation. Galaxies {D1, D2, D3} lose all of their halos and most of the stars in 6, 4.5, and 5 Gyr, respectively. As is the case with the large spirals, galaxy D2 from Cluster II experiences the strongest tidal heating, while galaxy D1 from Cluster I the weakest. The final state of the models is very peculiar. The particles are squeezed into a narrow “tube” stretching for several hundred kiloparsecs. The shape of the structure is truly one-dimensional; the axis ratios are smaller than a few percent. The orientation of the stream must be in the direction of the strongest component of the tidal force at the moment of disruption. Of course, such a long straight line is an artifact of the tidal approximation: in real clusters the tidal stream would bend and curve beyond a few tens of kpc.

These results are not inconsistent with the presence of dwarf galaxies in clusters. A continuous infall of small galaxies is expected. However once in the cluster, the diffuse dwarf spheroidals should be disrupted in several crossing times. In contrast, the dense dwarf ellipticals should be almost unaffected by tidal heating and might be found in any parts of the cluster.

6.2. Low Surface Brightness Galaxies

A much more luminous but even more diffuse type is the low surface brightness galaxies. LSB galaxies have slowly rising rotation curves and very extended disks compared to the high surface brightness spirals. McGaugh & de Blok (1998) find $R_0 \sim 10$ kpc as a representative scale length of galaxies in their sample. Nevertheless, the asymptotic values of the rotation curve of the high and low surface brightness galaxies are similar, and they both follow the same Tully-Fisher relation (Dalcanton et al. 1997b,a).

Similarly to dwarf spheroidals, the LSB galaxies are extremely sensitive to tidal heating. In order to investigate if they are also prone to destruction, I run three models {LSB1, LSB2, LSB3} varying the disk mass and scale length (Table 1). Each model is embedded in a massive halo. In model LSB1 the disk and the halo have the same masses as in galaxy L3 but spread out with $R_0 = 10$ kpc.

In model LSB2 the disk mass is reduced by a factor of 4 relative to LSB1. And in the extreme model LSB3 the scale length is further increased to $R_0 = 15$ kpc. The tidal history of all LSB models is the same as in galaxy L3.

Figure 12 shows the initial rotation curves for the three LSB models. Unlike Fig. 1, the x-axis scale is in kpc to emphasize the huge extent of these galaxies. Even though the halo mass is the same in all three models, the maximum value of the circular velocity declines from 229 km s^{-1} to 181 km s^{-1} as a result of the decreasing disk mass and increasing scale length. Dark matter dominates everywhere and determines the stability of stellar disks against tidal disruption. For galaxies LSB1 and LSB2 the average halo density in the core, $6 \times 10^{-3} M_{\odot} \text{pc}^{-3}$, is above the critical tidal density, but galaxy LSB3 with $\rho_{\text{av}}(R_c) = 1.7 \times 10^{-3} M_{\odot} \text{pc}^{-3}$ is not expected to survive.

Simulations again confirm the predictions based on the tidal density. Figure 13 shows that the halos of models LSB1 and LSB2 are truncated at about 30 kpc, similarly to model L3. For the LSB galaxies, however, this implies losing 70% of their dark mass (see Table 3). As a result, the circular velocity falls by 18% to 25%. Stellar disks are transformed even more strongly. Although only 20% of the stars are lost, the rest settle into a spheroidal configuration with comparable axis ratios in all directions. The radial scale length shrinks, while the vertical scale height expands by more than a factor of five. The density distribution is no longer exponential and declines more sharply (Figure 14). Any gas remaining in the diffuse disks would be stripped by ram pressure of the intracluster media. The likely outcome of such evolution is a gas-devoid spheroidal galaxy.

The third model, LSB3, is essentially disrupted by tidal forces. Only 4% of the halo remains bound at the end of the simulation. Because of the larger initial extent and lower density, the truncation radius is correspondingly smaller: $R_t \approx 30/1.5 = 20$ kpc (cf. Figure 13). The central density of the halo is reduced by more than a factor of four. Figure 14 shows that the stellar component is also severely damaged. The disk shrinks to less than a half of its original size and loses most of the stars. The surface density has fallen at all radii. This small remnant of the galaxy is unlikely to survive tidal

heating for much longer and will be torn apart by future tidal shocks.

To aid the comparison with observations, the critical tidal density (eq. [1]) can be translated to the projected surface brightness of the disk that would be disrupted by tidal forces. The face-on disks with the scale length $R_0 \sim 3$ kpc would satisfy the disruption condition $\rho_{\text{av}}(R_0) < \rho_{\text{tid}}$ if their central surface brightness in the B band is below

$$\mu_{\text{tid}} = 25.0 - 2.5 \log \left(\frac{F_{\text{tid}}}{100 \text{ Gyr}^{-2}} \right) \left(\frac{R_0}{3 \text{ kpc}} \right) \left(\frac{M/L_B}{2} \right)^{-1} \quad (31)$$

or $\mu_{\text{tid}} = 23.8 \text{ mag arcsec}^{-2}$ in the R band. For the edge-on disks the critical surface brightness can be up to a factor of 10 higher. However, if the dark matter cores are even denser ($\rho_{h,\text{av}} > \rho_{d,\text{av}}$) then μ_{tid} would correspondingly decrease. The discoveries in the Coma cluster of the giant diffuse arc with the surface brightness $\mu_B < 26.5 \text{ mag arcsec}^{-2}$ by Trentham & Mobasher (1998) and the diffuse plume-like feature with $\mu_R \approx 26 \text{ mag arcsec}^{-2}$ by Gregg & West (1998) may provide the examples of a complete tidal disruption.

6.3. Origin of Intracluster Light

Diffuse emission, not associated with galaxies, contributes 10% to 50% of the light from clusters (Burstein et al. 1995; Vilchez-Gomez 1999). As the tidal forces remove a substantial amount of stars from the low surface brightness galaxies, tidal streams stretch across the clusters. Is there enough LSB galaxies to provide the origin of diffuse intracluster light?

The fraction of stars stripped from the galaxies can be estimated as follows. Assume that the initial galaxy luminosity function is given by equation (2) and that the luminosity, along with the mass, scales linearly with the initial extent of the galaxy: $L \propto R$. Tidal truncation removes stars beyond the radius $R_t \approx R_{t,*} (\sigma_g/\sigma_{g,*})$, where $R_{t,*}$ is the tidal radius of L_* galaxies. Then the luminosity after truncation is $L_t = L(R_t/R) = L_*(R_{t,*}/R_*)(\sigma_g/\sigma_{g,*})$, and the fraction of dispersed light as a function of $x \equiv L/L_*$ is

$$f_d \equiv \frac{1}{L_{\text{tot}}} \frac{dL_{\text{lost}}}{d \log L} = \frac{L - L_t}{L_{\text{tot}}} N(L)L, \quad (32)$$

where the total luminosity of the cluster is $L_{\text{tot}} = \int N(L) L dL = N_0 L_* \Gamma(2 - \alpha)$. Using the adopted

luminosity function and the Faber-Jackson relation $\sigma_g = \sigma_{g,*} (L/L_*)^{1/4}$, the distribution becomes

$$f_d(x) = \frac{x^{1-\alpha}}{\Gamma(2-\alpha)} \left(x - \frac{R_{t,*}}{R_*} x^{1/4} \right) e^{-x}. \quad (33)$$

The simulations show that $R_{t,*} \approx 30$ kpc and the typical ratio $R_{t,*}/R_* = 0.2 - 0.5$. For $\alpha = 1 - 1.5$, the distribution peaks around the characteristic scale $x = 1$.

This calculation shows that most of the stripped stars come from giant L_* galaxies. Since the giants dominate the integrated light of both high and low surface brightness galaxies, the amount of the intracluster light in the tidal disruption scenario is proportional to the average fraction of LSB galaxies. The comparison of the APM survey and the CfA Redshift Survey (Sprayberry et al. 1997) shows that LSB galaxies contribute about 20% of the total light in the field. Dalcanton et al. (1997a) find that this fraction may even be higher. Also, in the Fornax cluster the LSB galaxies contain 20% to 30% of the total light (Kambas et al. 2000). Thus the disruption of large low surface brightness galaxies would naturally account for the intracluster light.

7. Comparison with Previous Work

The idea of transforming spirals into S0s by tidal heating in clusters is not new. From the study of galaxy collisions in cluster cores, Richstone (1976) finds that the dark matter halos are severely truncated. Simulations of the tidal heating of colliding galaxies (Farouki & Shapiro 1981) suggest that the disks grow in scale height, up to $z_0 \approx 0.2 R_0$. Despite the limitations of analytical cluster models and small number of particles, these early studies agree qualitatively with the more advanced computations.

A detailed investigation of galaxies in clusters has not been possible until very recently. Moore et al. (1996) and Moore, Lake & Katz (1998) have conducted the first high-resolution simulation of the tidal effects, using a singular isothermal cluster model populated by a large number of tidally-truncated galaxies. Both the neighbor galaxies and the cluster halo exerted tides on the galaxy simulated with higher resolution. Moore et al. predicted a strong evolution: the disks of medium size spirals ($V_c = 160 \text{ km s}^{-1}$) were destroyed

and transformed into dwarf spheroidals. Two effects may have contributed to this: (i) they used the cluster with a higher velocity dispersion (like Coma) where the tidal forces are stronger than in the clusters (like Virgo) simulated here, and (ii) the clusters growing hierarchically had less time to exert tidal effects than a steady massive cluster.

More recent simulations of Moore et al. (1999) have incorporated the hierarchical cluster formation in the $\Omega_0 = 1$ cosmology and indicate more moderate tidal evolution. They find that the disks of high surface brightness spirals survive within their dark matter halos but expand in vertical direction by a factor 2 to 3. Their new results are in a much better agreement with our models L1–L3.

Due to a smaller number of particles in the disk (2×10^4) and in the halo (5×10^4), Moore et al. (1999) simulations could suffer from numerical relaxation more strongly than our results. Estimating $m_h = 4 \times 10^6 M_\odot$, $\rho_h(R_c) \approx 0.2 M_\odot \text{pc}^{-3}$, $v_{\text{enc,h}} \approx 180 \text{ km s}^{-1}$ for their isolated HSB galaxy, I find the disk heating time $t_{\text{rel,h}} \sim 1.5 \text{ Gyr}$ (cf. eq. [25]). However, their Fig. 5 shows that in 5 Gyr the disk has expanded by only slightly more than a factor of 2, which corresponds to a relaxation time of 4.5 Gyr. Thus for some reason, in Moore’s simulation the numerical relaxation rate is three times slower. The only worrying sign is the steepening of the central density profile of the LSB galaxy in their Fig. 7. Since tidal heating vanishes in the center it cannot be responsible for this effect, which could instead be a manifestation of the artificial “core collapse”.

Moore et al. (1999) have examined the survival of the disks as a function of their mass, scale length, and the core radius of the surrounding dark matter halo. They find that compact disks are stable regardless of the halo core radius and that extended disks are stabilized by denser halos. All this can be explained in terms of a single tidal density parameter (cf. eq. [1]). The galaxies are stable if their combined inner density, of stars and dark matter, is above the tidal density. The results of Table 1 of Moore et al. (1999) indicate the truncation radius of about 20 kpc for small halo core radii ($R_c = 1 \text{ kpc}$) and about 10 kpc for large core radii ($R_c = 10 \text{ kpc}$), all of which correspond to a tidal density $\rho_{\text{tid}} \approx 3.6 \times 10^{-3} M_\odot \text{pc}^{-3}$. (The fraction of stars lost is independent of

the disk mass as long as the dark halo dominates, $M_d \ll M_h$.)

Despite different cluster models and simulation methods, the critical tidal densities in Moore et al. (1999) and in this paper agree within a factor of two, and the predicted dynamical evolution of galaxies is also similar. Some of the difference may be due to the close encounters of neighbor galaxies within $60 h^{-1} \text{ kpc}$, which are not resolved in my cluster simulations (Paper I estimates that these encounters contribute 10% to 50% of the overall tidal heating, I_{tid} , eq. [26]). Nevertheless, it is remarkable that such a simple concept as the tidal density of the Roche lobe provides a quantitatively accurate description of detailed simulations. It offers a direct way to compare the results of different authors.

Tidal disruption of galaxies as the origin of intracluster light has been envisioned by Merritt (1984). He argued that the most probable time for disruption is during the cluster collapse. Moore et al. (1999) also confirm the disruption of LSB galaxies in their simulations. Calcáneo-Roldán et al. (2000) present an excellent example of a diffuse arc structure in the Centaurus cluster and explain it with the debris of a low surface brightness galaxy disrupted by the giant elliptical NGC 4709. Their finding that the stripped stars produce diffuse features like those observed goes along with the results of §6. On a scale of the Local Group, Mayer et al. (2001) find that the observed dwarf spheroidal galaxies could be the remnants of tidally-disrupted LSB progenitors.

It should also be mentioned that Dubinski (1998) has combined the self-consistent cluster evolution with the galactic simulation in a single parallel tree-code run. He aimed to study the formation of a giant cD galaxy in the cluster center through a sequence of mergers of smaller galaxies. Unfortunately, his approach does not allow enough resolution to follow the dynamics of galaxies other than the central giant.

8. Discussion

The main result of this work is a natural and quantitative explanation of the transformation of spiral galaxies into S0s. The simulations show that even on the orbits with maximum expected tidal heating, large disk galaxies still remain flat-

tened and not elliptical. The evolution of elliptical galaxies must have proceeded prior to the cluster formation.

The main advance is made with the supporting simulations of the hierarchical cluster formation, reported in Paper I. The galactic orbits, the tidal field along them, and the timescales of dynamical evolution are all representative of the three plausible cosmological scenarios of structure formation. The evolution is stronger in the models ($\Omega_0 < 1$) where galaxies spend more time in the dense cluster environment.

Unlike previous studies with analytical cluster models, this work demonstrates that tidal heating is not limited to the cluster core because large local substructures are present in all parts of the forming clusters. In fact, most of the observable effects (halo truncation and disk heating) happen in the outer regions, as soon as the galaxy enters the cluster. Also, most of the evolution can be predicted using a single parameter, the critical tidal density along the orbit (eq. [1]).

A testable prediction of the tidally-driven evolution is the preferential abundance of S0 galaxies in the middle of large clusters at the expense of the spirals. Disk galaxies on the cluster periphery should have distorted profiles as well as the occasional spots of diminishing star formation. The abundance of elliptical galaxies, on the other hand, should be universal. These predictions are confirmed by observations (Jones, Smail & Couch 2000). A systematic study of galaxies at various stages of their evolution in clusters by the Sloan Digital Sky Survey (Blanton et al. 2002) will further improve the observational picture.

New HST images of the cluster CL 1358+62 (van Dokkum et al. 1998) show that the S0s are systematically bluer in the outer regions and may have formed stars more recently than the inner S0s. Interestingly, the brightest blue galaxies are bulge-dominated. Even though S0s are systematically less luminous than both ellipticals and spirals (van den Bergh 1998), their bulges may appear more prominent after star formation has ceased: the disks would dim by up to 2 mag, while the bulges would brighten due to the reduced extinction. These effects, however, may not be sufficient to explain the large bulges of S0s from the small bulges of Sa-Sc galaxies (Kent 1985). Therefore, like the elliptical galaxies, most of the bulges had

to accumulate at the early stages of galaxy formation.

The most significant limitation of the present study is the absence of gas dynamics. Future work should include a self-consistent treatment of the gas, both in the cluster and the galaxy simulations. Parallel Tree-SPH codes should be able to address this issue, although the amount of computations is very large. Also, high-resolution cluster simulations should help to resolve close galactic encounters. A nested grid method is necessary here, since the dynamical range should be extended by at least a factor of 10, from $60 h^{-1}$ kpc to less than $5 h^{-1}$ kpc. Adaptive mesh codes, such as AMR (Bryan et al. 1995), could reach the desired level but the computational expense is again not currently possible. The interpenetrating galaxy encounters may be responsible for the unexpected star formation episodes, such as in the “E+A” galaxies (Gunn 1989; Zabludoff 1999).

9. Conclusions

I have used the high-resolution N -body simulations to explore the dynamical evolution of disk galaxies in clusters. The evolution is driven by the tidal forces of the hierarchically forming clusters, extracted from the lower resolution simulations (Gnedin 2003) in three cosmological scenarios. I find that tidal effects are capable of inducing strong dynamical and morphological transformations, which can be parametrized by the critical tidal density along the galactic orbit. In the Virgo-type clusters this tidal density is $\rho_{\text{tid}} \sim 2 \times 10^{-3} M_{\odot} \text{pc}^{-3}$.

(i) Disks of large spiral galaxies thicken by a factor of two to three, while the stellar velocity dispersion in outer regions rises to 100 km s^{-1} . Toomre’s Q parameter increases to $\gtrsim 2$ and even a large amount of cold gas is unable to make the disks gravitationally unstable. The gas in the outer regions can be stripped by ram pressure of the intracluster gas. However, the stellar surface density distribution remains similar to the initial. Devoid of star formation these galaxies transform into the S0s, in agreement with the observations of low redshift clusters.

(ii) Dark matter halos are truncated at 30 ± 6 kpc, for the initial circular velocity of 250 km s^{-1} . In smaller halos the truncation radius is propor-

tionately smaller, $R_t \propto V_c$. As a result, the galaxies with extended halos may lose most of their mass to the cluster.

(iii) Low density (dwarf spheroidal and low surface brightness) galaxies entering the cluster may get completely disrupted by tidal shocks. The stripped material would stretch in long tidal streams along the original trajectories. According to the current faint galaxy surveys, the unbound stars of giant LSB galaxies may provide enough material for the diffuse intracluster light.

(iv) In all three cosmological models tidal heating is not limited to the cluster core and starts to affect galaxies as soon as they enter the cluster. The variation of the evolution on different orbits within the same cluster is as large as the variation due to the different cluster models. Nevertheless, the epoch of cluster formation, the critical tidal densities, and the heating rates indicate that the low Ω_0 models produce stronger dynamical evolution of galaxies and agree with observations better than the $\Omega_0 = 1$ model.

I would like to thank my thesis advisor J. P. Ostriker for his support and guidance, Martin Weinberg for discussions, Mike Blanton for his excellent Points visualization program, Lars Hernquist for the routines generating disk initial conditions and for the original version of the SCF code, and Jeremy Goodman, David Spergel, Neta Bahcall, Scott Tremaine, and George Lake for valuable comments. I acknowledge the support from NSF grant AST 94-24416. This work was submitted in partial fulfillment of the Ph.D. requirements at Princeton University.

REFERENCES

- Abadi, M. G., Moore, B., & Bower R. G. 1999, MNRAS, 308, 947
- Barnes, J. E., & Hernquist, L. 1996, ApJ, 471, 115
- Binney, J., & Merrifield, M. 1998, Galactic Astronomy (Princeton: Princeton University Press)
- Binney, J., & Tremaine, S. 1987, Galactic Dynamics (Princeton: Princeton University Press)
- Blanton, M. R., et al. 2002, ApJ, submitted; astro-ph/0209479
- Bryan, G. L., Norman, M. L., Stone, J. M., Cen, R., & Ostriker, J. P. 1995, Comp. Phys. Comm., 89, 149
- Burstein, D. 1979, ApJ, 234, 829
- Burstein, G. M., Nichol, R. C., Tyson, J. A., Ulmer, M. P., & Wittman, D. 1995, AJ, 110, 1507
- Calcáneo-Roldán, C., Moore, B., Bland-Hawthorn, J., Malin, D., & Sadler, E. M. 2000, MNRAS, 314, 324
- Cayatte, V., Kotanyi, C., Balkowski, C., & van Gorkom, J. H. 1994, AJ, 107, 1003
- Dalcanton, J. J., Spergel, D. N., Gunn, J. E., Schmidt, M., & Schneider, D. P. 1997a, AJ, 114, 635
- Dalcanton, J. J., Spergel, D. N., & Summers, F. J. 1997b, ApJ, 482, 659
- Dekel, A., & Silk, J. 1986, ApJ, 303, 39
- de Vaucouleurs, G., & Freeman, K. C. 1972, Vistas in Astronomy, 14, 163
- Driver, S. P., Couch, W. J., & Phillipps, S. 1998, MNRAS, 301, 369
- Dubinski, J. 1998, ApJ, 502, 141
- Edvardsson, B., Andersen, J., Gustafsson, B., Lambert, D.L., Nissen, P.E., & Tomkin, J. 1993, A&A, 275, 101
- Ellis, R. S., Smail, I., Dressler, A., Couch, W. J., Oemler, A., Butcher, H., & Sharples, R. 1997, ApJ, 483, 582
- Faber, S. M., & Jackson, R. E. 1976, ApJ, 204, 668
- Fabian, A. C., & Daines, S. J. 1991, MNRAS, 252, 17P
- Farouki, R., & Shapiro, S. L. 1981, ApJ, 243, 32
- Ferguson, H. C., & Binggeli, B. 1994, A&A Rev., 6, 67
- Gallagher, J. S. III, & Wyse, R. F. G. 1994, PASP, 106, 1225
- Ghigna, S., Moore, B., Governato, F., Lake, G., Quinn, T., & Stadel, J. 1998, MNRAS, 300, 146

- Gnedin, O. Y. 2003, *ApJ*, 582, 141 (Paper I)
- Gnedin, O. Y., Hernquist, L., & Ostriker J. P. 1999, *ApJ*, 514, 109
- Gnedin, O. Y., & Ostriker, J. P. 1999, *ApJ*, 513, 626
- Gnedin, O. Y., & Zhao, H.S. 2002, *MNRAS*, 333, 299
- Gregg, M. D., & West, M. J. 1998, *Nature*, 396, 549
- Gunn, J. E. 1989, in *The Epoch of Galaxy Formation*, eds. C. S. Frenk et al. (Dordrecht: Kluwer)
- Gunn, J. E., & Gott, J. R. III 1972, *ApJ*, 176, 1
- Hank Donnelly, R., Markevitch, M., Forman, W., Jones, C., Churazov, E., & Gilfanov, M. 1999, *ApJ*, 513, 690
- Hernquist, L. 1993, *ApJS*, 86, 389
- Hernquist, L., & Mihos, J. C. 1995, *ApJ*, 448, 41
- Hernquist, L., & Ostriker, J. P. 1992, *ApJ*, 386, 375
- Jog, C. J., & Solomon, P. M. 1984, *ApJ*, 276, 114
- Jones, C., & Forman, W. 1984, *ApJ*, 276, 38
- Jones, L., Smail, I., & Couch, W. J. 2000, *ApJ*, 528, 118
- Kambas, A., Davies, J. I., Smith, R. M., Bianchi, S., & Haynes, J. A. 2000, *AJ*, 120, 1316
- Kennicutt, R. C. 1998, *ARA&A*, 36, 189
- Kent, S. M. 1985, *ApJS*, 59, 115
- Kormendy, J. 1985, *ApJ*, 295, 73
- Kritsuk, A. G. 1983, *Astrophysics*, 19, 263
- Lacey, C. G. 1984, *MNRAS*, 208, 687
- Lacey, C. G., & Ostriker, J. P. 1985, *ApJ*, 299, 633
- Mayer, L., Governato, F., Colpi, M., Moore, B., Quinn, T., Wadsley, J., Stadel, J., & Lake, G. 2001, *ApJ*, 559, 754
- McGaugh, S. S., & de Blok, W. J. G. 1998, *ApJ*, 499, 41
- Merritt, D. 1984, *ApJ*, 276, 26
- Moore, B., Katz, N., Lake, G., Dressler, A., & Oemler, A. 1996, *Nature*, 379, 613
- Moore, B., Lake, G., & Katz, N. 1998, *ApJ*, 495, 139
- Moore, B., Lake, G., Quinn, T., & Stadel, J. 1999, *MNRAS*, 304, 465
- Moss, C., & Whittle, M. 1993, *ApJ*, 407, L17
- Phillipps, S., Driver, S. P., Couch, W. J., & Smith, R. M. 1998, *ApJ*, 498, L119
- Quilis, V., Moore, B., & Bower, R. 2000, *Science*, 288, 1617
- Richstone, D. O. 1976, *ApJ*, 204, 642
- Roettiger, K., Loken, C., & Burns, J. O. 1997, *ApJS*, 109, 307
- Rybicki, G. B. 1971, *Ap&SS*, 14, 15
- Sandage, A. 1961, *The Hubble Atlas of Galaxies* (Washington, DC: Carnegie Institution of Washington)
- Sarazin, C. L. 1988, *X-ray emission from clusters of galaxies* (Cambridge: Cambridge University Press), p. 216
- Seifert, W., & Scorza, C. 1996, *A&A*, 310, 75
- Sellwood, J. A. 1987, *ARA&A*, 25, 151
- Sellwood, J. A. 1999, in *ASP Conf. Ser. 182, Galaxy Dynamics*, ed. D. R. Merritt, M. Valuri & J. A. Sellwood (San Francisco: ASP), 96
- Simien, F., & Prugniel, Ph. 1998, *A&AS*, 131, 287
- Spitzer, L. Jr, & Hart, M. H. 1971, *ApJ*, 164, 399
- Sprayberry, D., Impey, C. D., Irwin, M. J., & Bothun, G. D. 1997, *ApJ*, 482, 104
- Springel, V., Yoshida, N., & White, S. D. M. 2001, *New Astronomy*, 6, 79
- Toomre, A. 1964, *ApJ*, 139, 1217
- Trentham, N., & Mobasher, B. 1998, *MNRAS*, 293, 53

- Tyson, J. A., Kochanski, G. P., & Dell'Antonio, I. P. 1998, *ApJ*, 498, L107
- Valluri, M., & Jog, C. J. 1991, *ApJ*, 374, 103
- van den Bergh, S. 1998, *Galaxy Morphology and Classification* (Cambridge: Cambridge University Press)
- van Dokkum, P. G., Franx, M., Kelson, D. D., Illingworth, G. D., Fisher, D., & Fabricant, D. 1998, *ApJ*, 500, 714
- Vílchez-Gómez, R. 1999, in *ASP Conf. Ser. 170, Low Surface Brightness Universe*, ed. J. I. Davies, C. Impey & S. Phillipps (San Francisco: ASP), 349
- Weinberg, M. D. 1993, *ApJ*, 410, 543
- Weinberg, M. D. 1996, *ApJ*, 470, 715
- Zabludoff, A. I. 1999, in *IAU Symp. 186, Galaxy Interactions at Low and High Redshift*, ed. J. E. Barnes & D. B. Sanders (Dordrecht: Kluwer), 125

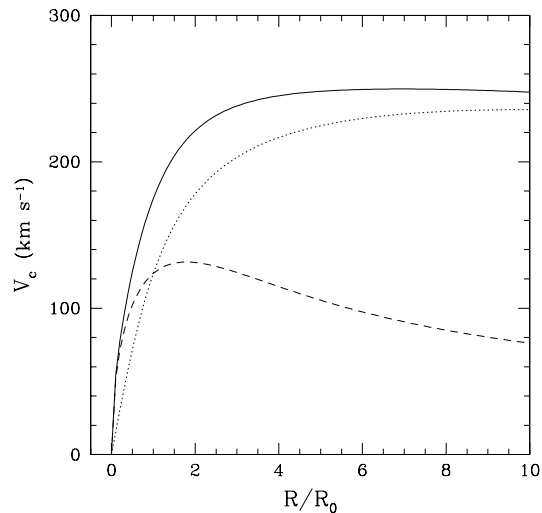


Fig. 1.— Initial rotation curve of large disk galaxies (solid line) and the individual contributions from the exponential disk (dashes) and the isothermal halo (dots). Cylindrical radius is in units of the disk scale length, R_0 .

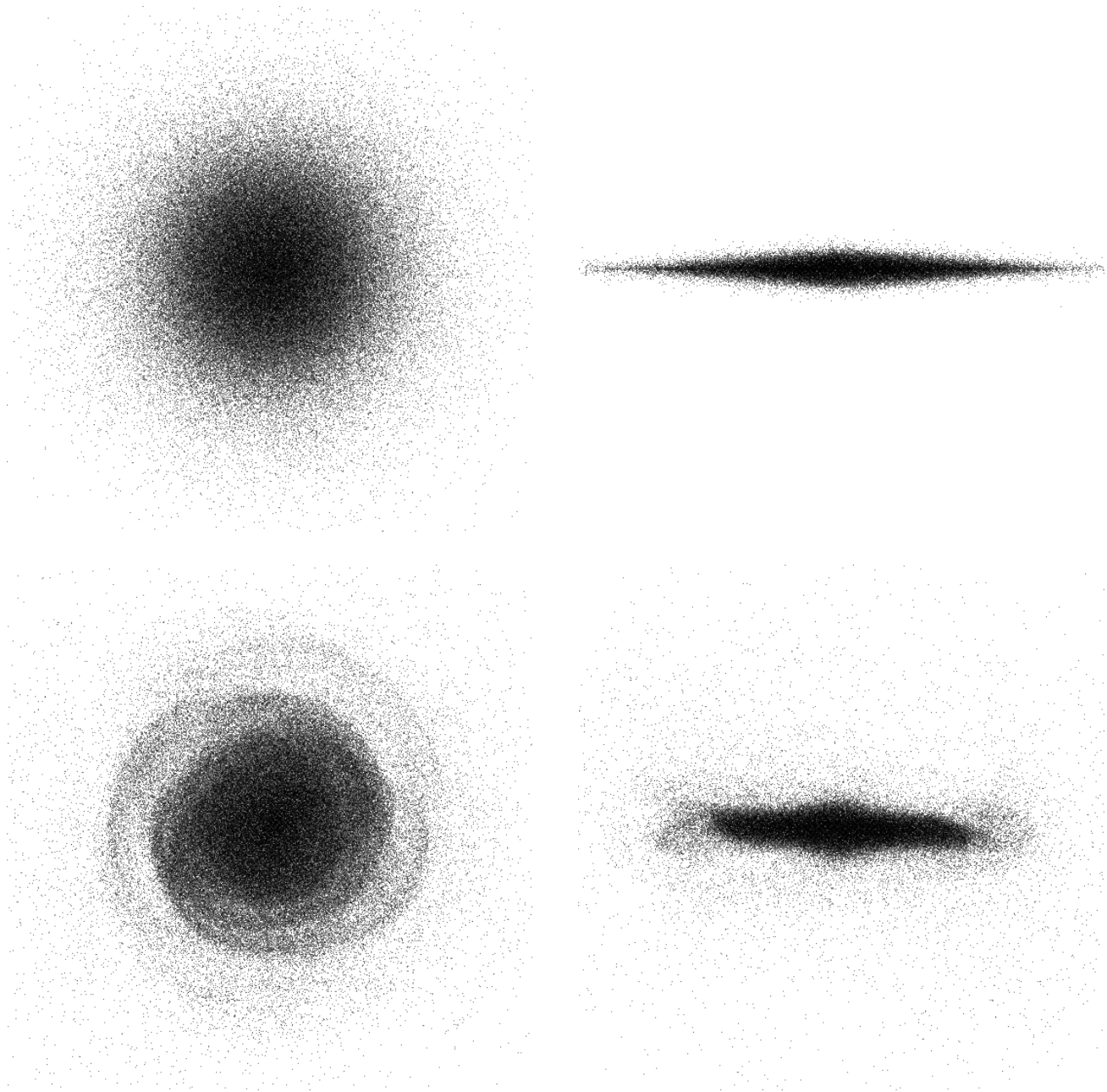


Fig. 2.—Upper panels: Initial conditions for large disk galaxies, face-on and edge-on views (only stellar particles are shown). Lower panels: Final configuration of galaxy L1.

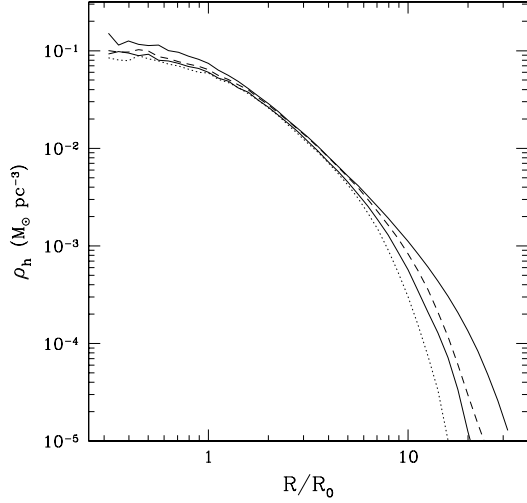


Fig. 3.— Halo density profiles of large galaxies L1 (dashes), L2 (dots), and L3 (solid line) at the end of each simulation. Outer thin line shows the initial distribution.

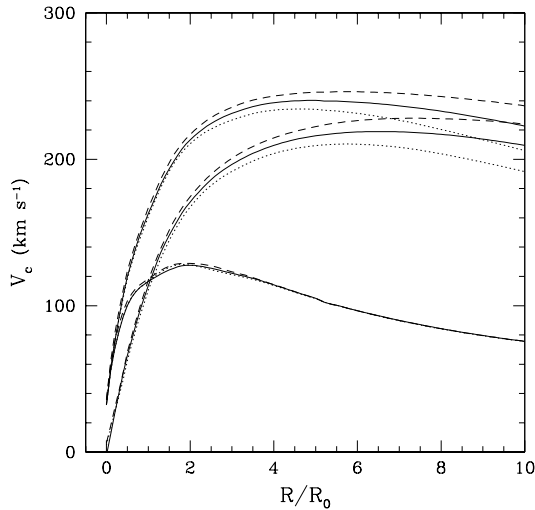


Fig. 4.— Rotation curves, with the disk and halo contributions, of large galaxies L1 (dashes), L2 (dots), and L3 (solid lines) at the end of each simulation.

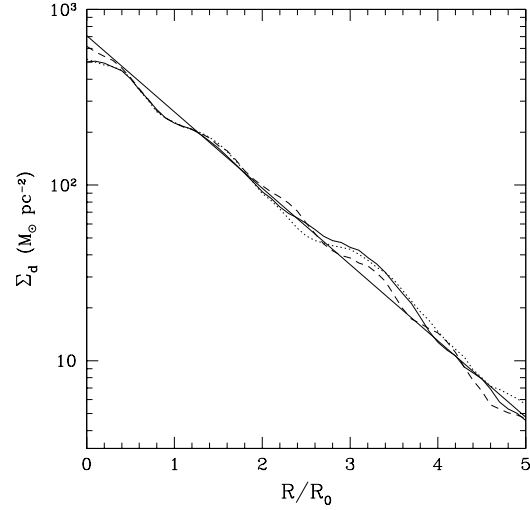


Fig. 5.— Disk surface density of large galaxies L1 (dashes), L2 (dots), and L3 (solid line) at the end of each simulation. Straight thin line shows the initial exponential profile.

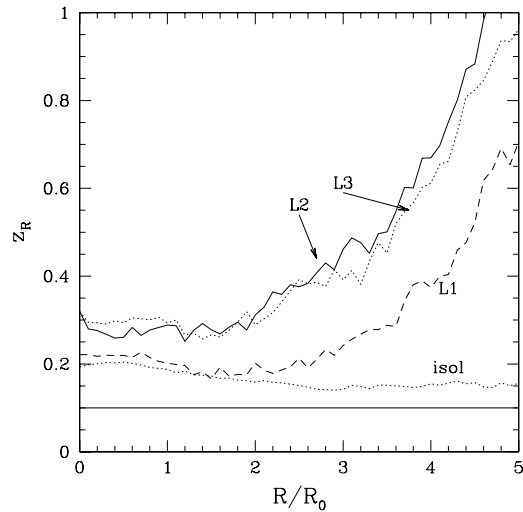


Fig. 6.— Disk scale height, z_0/R_0 , as a function of cylindrical radius for large galaxies L1 (dashes), L2 (dots), and L3 (solid line) at the end of each simulation. Declining dotted line shows the numerical heating in the isolated run. Solid horizontal line is the initial scale height, $0.1 R_0$.

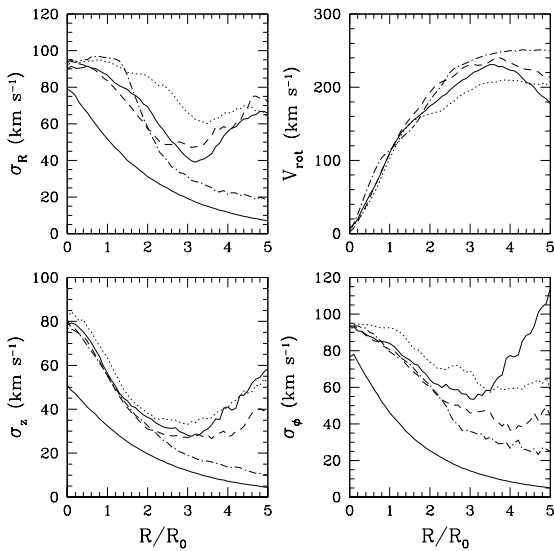


Fig. 7.— Three components of the velocity dispersion, σ_R , σ_ϕ , σ_z , and the rotation speed V_{rot} of the disks of large galaxies L1 (dashes), L2 (dots), and L3 (solid line) at the end of each simulation. Dash-dotted line is for the isolated run. Thin solid lines in the three dispersion panels show the initial state of the disk.

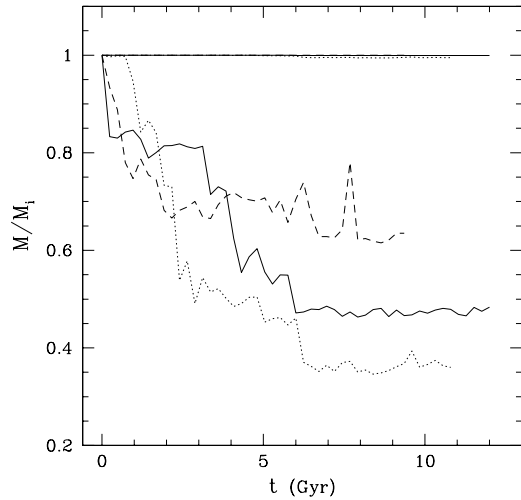


Fig. 8.— The disk and halo masses of large galaxies L1 (dashes), L2 (dots), and L3 (solid line) versus time. Disk masses are essentially constant (horizontal lines). Halo masses drop steadily (declining lines), although the instantaneous amount of bound mass may fluctuate with the external potential. Note that simulation times differ for each cosmological model. Sudden mass losses can be identified with the peaks of the external tidal force (cf. Figs. 14–16 in Paper I): at $t = 0.3, 0.8, 1.2$ Gyr for L1, at $t = 1.8, 2.2, 2.8, 6$ Gyr for L2, and at $t = 0.1, 1.4, 3.3, 4.2, 5.1$ Gyr for L3.

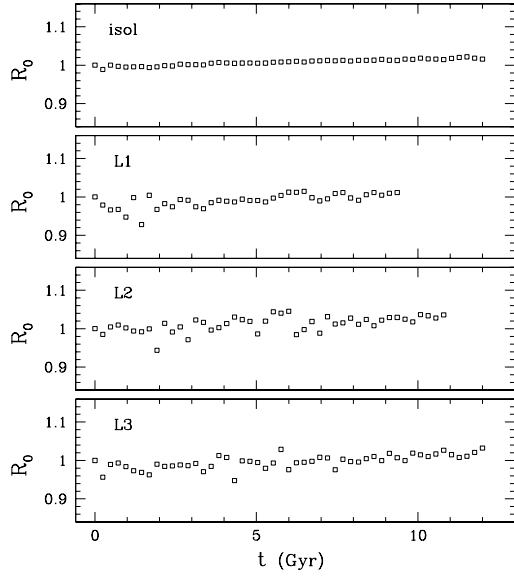


Fig. 9.— Variation of the disk scale length with time for large galaxies L1, L2, L3 and for the isolated run.

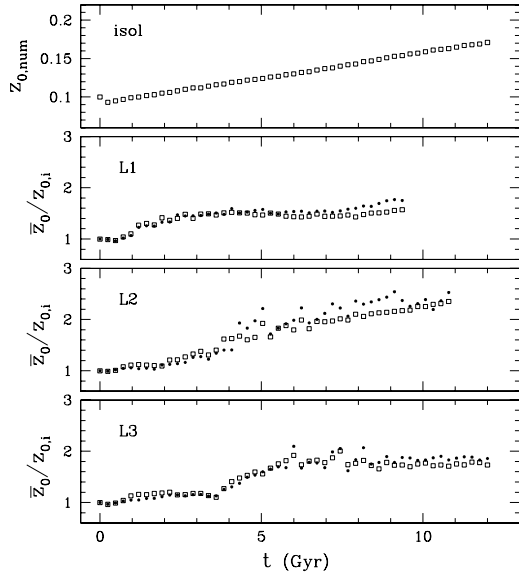


Fig. 10.— Variation of the global scale height with time for large galaxies L1, L2, L3 and for the isolated run. In the three lower panels, the instantaneous value of the scale height is normalized to the initial value and corrected for the effect of numerical heating (eq. [13]). Small dots show for comparison the results of GADGET simulations with more accurate vertical forces but with $N_d = 10^5$, $N_h = 4 \times 10^5$ particles.

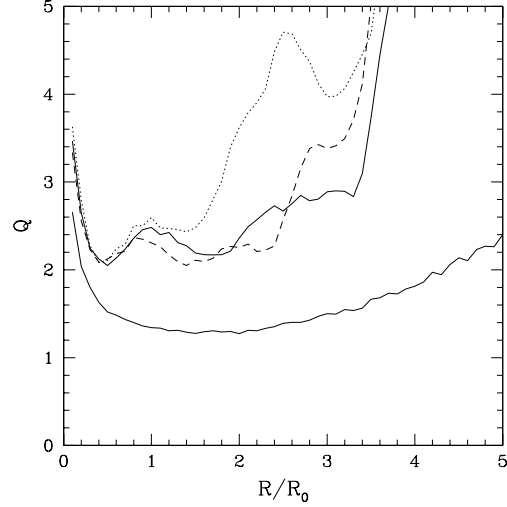


Fig. 11.— Toomre's Q parameter for the disks of large galaxies L1 (dashes), L2 (dots), L3 (solid line) at the end of each simulation. Lower solid line shows the initial state of the disk.

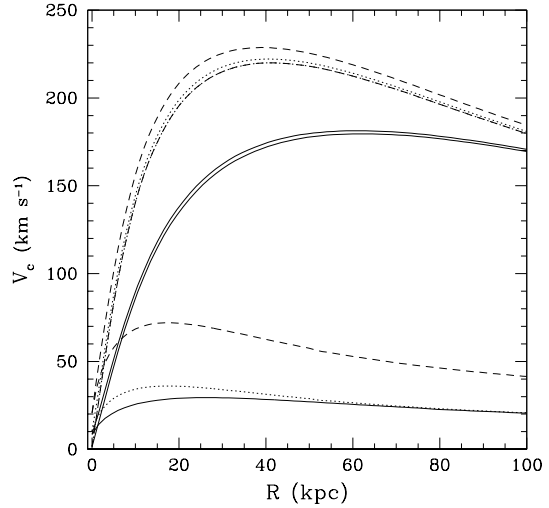


Fig. 12.— Initial rotational curves, with the disk and halo contributions, of the low surface brightness galaxies LSB1 (dashes), LSB2 (dots), LSB3 (solid line).

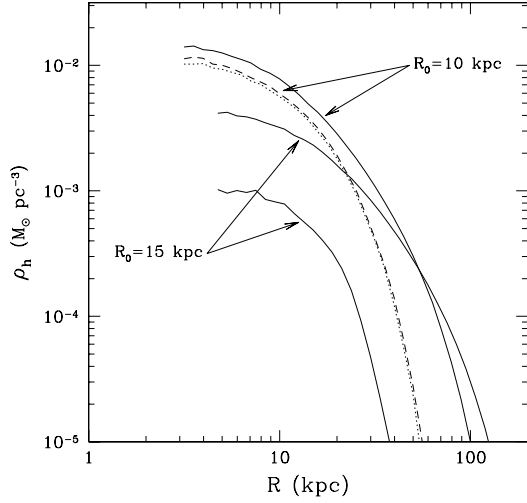


Fig. 13.— Final halo density profiles of galaxies LSB1 (dashes), LSB2 (dots), LSB3 (thick solid line). Thin solid lines show the initial profiles for each galaxy.

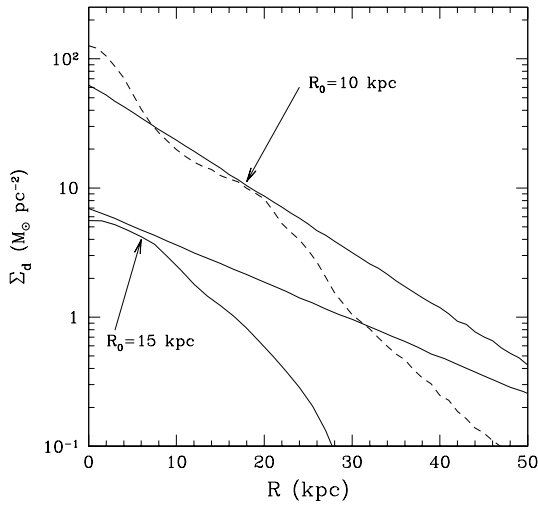


Fig. 14.— Final disk surface density of galaxies LSB1 (dashes) and LSB3 (thick solid line). Thin solid lines show the initial profiles for each galaxy.

TABLE 1
INITIAL PARAMETERS OF SIMULATED GALAXIES

Model	M_h (M_\odot)	M_d (M_\odot)	V_c (km s^{-1})	R_0 (kpc)	z_0 (kpc)	T_{rot} (yr)
L1,L2,L3	8×10^{11}	4×10^{10}	250	3	0.3	1.2×10^8
D1,D2,D3	2×10^9	10^8	20	1	0.1	5.0×10^8
LSB1	8×10^{11}	4×10^{10}	229	10	1	4.6×10^8
LSB2	8×10^{11}	10^{10}	222	10	1	4.7×10^8
LSB3	8×10^{11}	10^{10}	181	15	1.5	7.0×10^8

TABLE 2A
ISOLATED RUNS

Model	N_d	N_h	Δt (yr)	$R_0/R_{0,i}$	$z_0/z_{0,i}$	b/a	c/a
L-isol	10^6	10^6	1.2×10^6	1.04	1.7	0.99	0.97
L-isol1	10^6	10^6	2.4×10^6	1.06	2.1	1.00	0.97
L-isol2	5×10^5	5×10^5	1.2×10^6	1.04	1.9	1.00	0.97
L-isol3	5×10^5	10^6	1.2×10^6	1.04	1.9	0.99	0.97
LSB-isol3	10^6	10^6	7.0×10^6	1.01	0.8	1.00	0.88

TABLE 2B
ENERGY CHANGES IN ISOLATED RUNS

Model	$\langle \Delta E/E \rangle_d$	$\langle (\Delta E/E)^2 \rangle_d$	$\langle (\Delta E/E)^2 \rangle_h$	$\langle \Delta E_z \rangle / \langle E_z \rangle_d$
L-isol	1.3×10^{-3}	4.8×10^{-3}	1.3×10^{-3}	1.0
L-isol1	-1.5×10^{-2}	1.1×10^{-2}	2.1×10^{-3}	1.1
L-isol2	2.6×10^{-3}	7.2×10^{-3}	1.7×10^{-3}	1.1
L-isol3	4.9×10^{-3}	7.9×10^{-3}	1.6×10^{-3}	1.2
LSB-isol3	3.2×10^{-2}	3.1×10^{-4}	1.2×10^{-3}	0.55

TABLE 3
FINAL PARAMETERS OF LARGE GALAXIES

Model	T_{sim} (Gyr)	$M_h/M_{h,i}$	$M_d/M_{d,i}$	$V_c/V_{c,i}$	$R_0/R_{0,i}$	$\bar{z}_0/z_{0,i}$	b/a	c/a
L1	9.35	0.63	1.000	0.98	1.01	1.6	0.93	0.88
L2	10.71	0.36	0.995	0.94	1.04	2.4	0.93	0.88
L3	12.28	0.48	0.999	0.95	1.03	1.7	0.89	0.84
L3a	12.28	0.55	1.000	0.99	1.01	1.4	0.92	0.87
L3b	12.28	0.39	0.997	0.93	1.02	2.5	0.91	0.88
LSB1	12.28	0.34	0.81	0.82	0.74	5.7	0.86	0.84
LSB2	12.28	0.32	0.77	0.75	0.78	5.2	0.87	0.79
LSB3	12.28	0.04	0.28	0.29	0.43	2.4	0.79	0.72

TABLE 4
TEST MODELS OF GALAXY L3

Model	N_d	N_h	Δt (yr)	$M_h/M_{h,i}$	$M_d/M_{d,i}$	$V_c/V_{c,i}$	$R_0/R_{0,i}$	$\bar{z}_0/z_{0,i}$	b/a	c/a
main	10^6	10^6	1.2×10^6	0.48	0.999	0.95	1.03	1.7	0.89	0.84
1	10^6	10^6	2.4×10^6	0.49	0.998	0.95	1.08	1.9	0.89	0.85
2	5×10^5	5×10^5	1.2×10^6	0.48	0.999	0.95	1.04	1.7	0.89	0.85
3	5×10^5	10^6	1.2×10^6	0.48	0.999	0.95	1.04	1.5	0.89	0.84

TABLE 5
GADGET RUNS

Model	N_d	N_h	$M_h/M_{h,i}$	$M_d/M_{d,i}$	$V_c/V_{c,i}$	$R_0/R_{0,i}$	$\bar{z}_0/z_{0,i}$	b/a	c/a
L1-GADGET	10^5	10^5	0.63	0.999	0.90	1.15	2.1	0.90	0.89
L2-GADGET	10^5	10^5	0.36	0.994	0.84	1.10	3.1	0.94	0.87
L3-GADGET	10^5	10^5	0.45	0.999	0.83	1.18	2.8	0.93	0.91
L1-GADGET	10^5	4×10^5	0.63	0.999	0.90	1.12	1.8	0.90	0.89
L2-GADGET	10^5	4×10^5	0.36	0.994	0.84	1.11	2.5	0.95	0.88
L3-GADGET	10^5	4×10^5	0.45	0.999	0.83	1.20	1.9	0.92	0.90